Atmos. Chem. Phys. Discuss., 15, 3493–3575, 2015
www.atmos-chem-phys-discuss.net/15/3493/2015/
doi:10.5194/acpd-15-3493-2015

Atmospheric Chemistry and Physics Discussions

Predicting the mineral composition of dust aerosols – Part 1: Representing key processes

J. P. Perlwitz[1,2,*], **C. Pérez García-Pando**[1,2,*], **and R. L. Miller**[2,1,*]

[1]Department of Applied Physics and Applied Mathematics, Columbia University in The City of New York, New York, USA
[2]NASA Goddard Institute for Space Studies, New York, New York, USA
[*]These authors contributed equally to this work.

Received: 17 December 2014 – Accepted: 30 December 2014 – Published: 6 February 2015

Correspondence to: J. P. Perlwitz (jan.p.perlwitz@nasa.gov)

Published by Copernicus Publications on behalf of the European Geosciences Union.

Abstract

Soil dust aerosols created by wind erosion are typically assigned globally uniform physical and chemical properties within Earth system models, despite known regional variations in the mineral content of the parent soil. Mineral composition of the aerosol particles is important to their interaction with climate, including shortwave absorption and radiative forcing, nucleation of cloud droplets and ice crystals, coating by heterogeneous uptake of sulfates and nitrates, and atmospheric processing of iron into bioavailable forms that increase the productivity of marine phytoplankton. Here, aerosol mineral composition is derived by extending a method that provides the composition of a wet-sieved soil. The extension accounts for measurements showing significant differences between the mineral fractions of the wet-sieved soil and the resulting aerosol concentration. For example, some phyllosilicate aerosols are more prevalent at silt sizes, even though they are nearly absent in a soil whose aggregates are dispersed by wet sieving during analysis. We reconstruct the undispersed size distribution of the original soil that is subject to wind erosion. An empirical constraint upon the relative emission of clay and silt is applied that further differentiates the soil and aerosol mineral composition. In addition, a method is proposed for mixing minerals with small impurities composed of iron oxides. These mixtures are important for transporting iron far from the dust source, because pure iron oxides are more dense and vulnerable to gravitational removal than most minerals comprising dust aerosols. A limited comparison to measurements from North Africa shows that the extension brings the model into better agreement, consistent with a more extensive comparison to global observations as well as measurements of elemental composition downwind of the Sahara, as described in companion articles.

1 Introduction

Climate perturbations by soil dust aerosols created by wind erosion depend fundamentally upon the physical and chemical properties of the aerosol particles. However, Earth

ACPD
15, 3493–3575, 2015

system models typically assume that soil dust aerosols have globally uniform composition, despite known regional variations in the mineral composition of the parent soil. Perturbations by dust to the energy and water cycles depend upon aerosol radiative forcing (Miller et al., 2004, 2014; Perlwitz and Miller, 2010), whose solar component is strongly related to the presence of iron oxides (Sokolik and Toon, 1996, 1999; Tegen et al., 1997; Redmond et al., 2010; Wagner et al., 2012; Moosmüller et al., 2012). Forcing at thermal wavelengths also varies with source mineral content (Turner, 2008). Absorption of solar radiation by dust alters the photolysis of ozone (Bian et al., 2003), while influencing chemical reactions of other trace gases (Goodman et al., 2000; Usher et al., 2003; Chen et al., 2011). The rates of heterogeneous chemical reactions on the dust particle surface that form coatings of sulfate, nitrate, chloride, or organics during atmospheric transport depend on the dust mineral and chemical composition (Dentener et al., 1996; Russell et al., 2002; Bian and Zender, 2003; Krueger et al., 2004; Sullivan et al., 2007; Matsuki et al., 2010; Rubasinghege et al., 2013). Dust aerosols influence cloud formation (and the associated radiative forcing) by serving as nucleation sites for cloud droplets and ice crystals (Johnson, 1982; Feingold et al., 1999; Sassen, 2002; DeMott et al., 2003; Twohy et al., 2009; Seifert et al., 2010). The nucleation properties of dust depend upon their hygroscopicity and shape, that in turn depend upon their mineral composition (Frinak et al., 2005; Kelly et al., 2007; Hatch et al., 2008; Ma et al., 2012; Hatch et al., 2014; Zimmermann et al., 2008; Hoose and Möhler, 2012; Murray et al., 2012; Atkinson et al., 2013; Yakobi-Hancock et al., 2013). Bioavailable iron within dust, transported to remote regions and processed during transport (Shi et al., 2011; Takahashi et al., 2011; Ito, 2012), fertilizes ocean phytoplankton, influencing carbon dioxide uptake and the global carbon cycle (Jickells et al., 2005; Maher et al., 2010; Shi et al., 2012; Schulz et al., 2012). Dust is associated with respiratory and cardiovascular disease, along with epidemics of meningoccocal meningitis in the African Sahel (Pérez García-Pando et al., 2014a, b), where iron from dust particles may foster bacterial growth and weaken the immune system.

ACPD
15, 3493–3575, 2015

Deriving aerosol mineral composition requires global maps derived from measured regional variations of soil mineral content. Claquin et al. (1999) proposed that the soil mineral fractions are approximately related to the soil type, which is available from global atlases (see also Nickovic et al., 2012; Journet et al., 2014). However, Claquin et al. (1999) noted that the mineral content of the emitted aerosol may differ from that of the parent soil for two reasons. First, measurements of mineral fractions are based upon wet sedimentation (or "wet sieving") techniques that disturb the soil sample, breaking aggregates that are found in the original, undispersed soil that is subject to wind erosion. Wet sieving alters the soil size distribution, replacing aggregates with a collection of smaller particles (Shao, 2001; Choate et al., 2006; Laurent et al., 2008). Second, certain particle sizes (and the minerals comprising these particles) are preferentially emitted and converted into aerosols. Size-resolved measurements show that silt sizes are emitted in greater proportion compared to clay (e.g. Gillette et al., 1974; Sow et al., 2009; Kok, 2011). Emission of minerals like phyllosilicates that are commonly found in aggregates will be underestimated where the aggregates are fragmented during wet sieving.

The challenge remains to derive mineral fractions of the emitted dust based upon their fractions measured in wet-sieved soils. Previous attempts to predict the aerosol mineral composition have generally neglected the effects of wet sieving (Hoose et al., 2008; Atkinson et al., 2013; Journet et al., 2014). Calculation of how the particle size distribution and mineral composition of the soil are modified during emission is also complicated (e.g. Shao, 2001; Alfaro and Gomes, 2001; Grini et al., 2002), although recent studies have proposed simplifications (Kok, 2011; Scanza et al., 2015). Finally, representations of aerosol mineral composition need to account for mixtures of minerals. Examination of individual particles shows that iron, an element that is central to many climate processes, is often found as trace impurities of iron oxide attached to aggregates of other minerals (Reid et al., 2003; Scheuvens et al., 2011; Lieke et al., 2011; Deboudt et al., 2012; Scheuvens and Kandler, 2014).

ACPD
15, 3493–3575, 2015

In this article, we extend previous models of dust mineral composition to address these challenges. Some of the extensions of our model have been introduced previously (Kok, 2011; Scanza et al., 2015). In Sect. 2, we reconstruct the undispersed soil size distribution of each mineral and calculate its modification during emission. We also calculate mixtures containing iron oxides to account for the transport of iron to remote regions. In Sect. 3, we describe simulations with the NASA Goddard Institute for Space Studies (GISS) Earth System ModelE that show the effect of our extensions. In Sect. 4, we describe the geographical distribution of emission and surface concentration for each mineral and its mixture with iron oxide, while using an intermediate model version to identify the origin of improved behavior in our new model, documented here and in the companion articles. We summarize the new features of our model in Sect. 5.

Our model extensions are motivated by observations. In Sect. 4, we show that our new model is in better agreement with aerosol measurements at a site in North Africa after correcting for the effects of wet sieving. Detailed comparison of the model to a broader array of observations is deferred to companion articles. In Perlwitz et al. (2015), we compare our predicted aerosol distribution to a new global compilation of mineral measurements from nearly sixty studies. In Pérez García-Pando et al. (2015), we evaluate our results using observations from the Izaña Observatory, where elemental composition of Saharan dust has been measured for the past decade.

2 The mineralogical dust cycle model

2.1 Overview

2.1.1 Modeling challenges

Our aim is to predict regional variations of aerosol mineral composition as a function of particle size. For comparison, ModelE currently predicts the size distribution of dust aerosols, but assumes a globally uniform mineral content (Miller et al., 2006). Regional

ACPD
15, 3493–3575, 2015

variations in soil mineral composition lead to variations in dust aerosol composition. However, deriving aerosol mineral content also requires knowledge of the size distribution of the parent soil along with its transformation during the emission process. Here, we discuss some of these challenges, before describing our algorithm in Sect. 2.2.

Claquin et al. (1999) proposed that soil mineral content is related to the soil type provided by the Digital Soil Map of the World (DSMW), compiled by the Food and Agriculture Organization (FAO) of the United Nations (FAO, 1995, 2007). For the clay-sized fraction of the soil (with particle diameters up to 2 µm), the DSMW soil type is used to estimate the fractional composition of phyllosilicates (illite, kaolinite and smectite) along with calcite and quartz. Similarly, for the silt-sized soil fraction (with diameters between 2 and 50 µm), soil type is used to estimate the fractional composition of calcite, quartz, feldspar, gypsum and hematite. These minerals were chosen because of their relative abundance and potential importance to climate and biogeochemical processes, although other minerals are present in arid soils. The relation between soil type and fractional mineral abundance within the clay and silt-size categories is summarized in the Mean Mineralogical Table (MMT; Table 2 from Claquin et al., 1999). Subsequent studies have refined the proposed relation between soil type and mineral composition (Nickovic et al., 2012; Journet et al., 2014). Estimating the soil mineral composition additionally requires information about the fraction of clay and silt-sized particles present at each location, available from global databases of soil texture (Webb et al., 1993; Reynolds et al., 2000; Shangguan et al., 2014).

Claquin et al. (1999) note that their MMT introduces two sources of uncertainty for dust aerosol modeling. First, the relation between mineral composition and soil type is derived from a limited amount of measurements that are particularly scarce in the arid and semi-arid areas that contain dust sources. Second, measurements are based on wet sedimentation ("wet sieving") techniques that disturb the soil samples, breaking the aggregates that are found in the original, undispersed soil that is subject to wind erosion. Wet sieving alters the soil size distribution, replacing aggregates with a collection of smaller and relatively loose particles (Shao, 2001; Choate et al., 2006; Laurent et al.,

ACPD
15, 3493–3575, 2015

2008). Techniques that minimize the breaking of the aggregates (McTainsh et al., 1997; Marticorena et al., 1997) are available to characterize the size distributions of North African and Chinese soil samples (Chatenet et al., 1996; Mei et al., 2004). However, these measurements remain very limited, are based upon a variety of analytical methods (Laurent et al., 2008), and provide the size distribution of only the bulk soil rather than distinguishing among individual minerals. Wet sieving is also used to characterize the soil texture in global datasets that give the fraction of clay, silt and sand-sized particles at each location (e.g. Shangguan et al., 2014). Claquin et al. (1999) emphasize that differences of the mineral size distribution between wet-sieved soils and the original undispersed soil that undergoes mobilization are potentially important and merit further examination. In the absence of knowledge about this difference, previous studies have assumed that the emitted size distribution of each mineral closely resembles that of the wet-sieved soil (Claquin et al., 1999; Hoose et al., 2008; Atkinson et al., 2013; Journet et al., 2014).

Modification of the soil size distribution by wet sieving and during emission is potentially large. Figure 1 shows the mass distribution as a function of particle size for common airborne minerals at Tinfou, Morocco during the Saharan Mineral Dust Experiment (SAMUM) campaign of 2006 (Kandler et al., 2009). Calculation of these distributions is described in page 2 of the Supplement and is based upon measurements of collections of aerosol particles that are sorted by size. Each particle consists of a single mineral or aggregates of different minerals. For example, images suggest that iron oxides are consistently present both in pure crystalline form and as small impurities attached to other minerals (e.g. Fig. 2.1f and g of Scheuvens and Kandler, 2014). The measurements are sorted between conditions of high and low aerosol concentration. The main difference between the two conditions is that larger-sized particles are missing from the low-concentration events (Fig. 1, top row), suggesting that these particles have been removed during gravitational settling following their mobilization at a distant source. In contrast, the presence of larger particles at times of high concentration (Fig. 1, bot-

ACPD
15, 3493–3575, 2015

tom row) suggests that this size distribution is a better indicator of the emitted size distribution.

Figure 1 shows that the mass of phyllosilicates like illite and kaolinite is predominately within silt particle sizes. That is, the phyllosilicates that are nominally "clay" minerals are observed mainly within larger silt-sized aerosols. This is corroborated by measurements at other locations where clay particles and aggregates routinely exceed 2 µm in particle diameter (e.g., Leinen et al., 1994; Reid et al., 2003; Alastuey et al., 2005; Jeong and Nousiainen, 2014). Wet sieving breaks up these larger particles, and models that do not account for this potentially allow a significant fraction of phyllosilicates to disperse unrealistically far from their source by underestimating gravitational deposition. This has implications for the delivery of phyllosilicate iron to fertilize photosynthesis within distant marine ecosystems (Journet et al., 2008).

The presence of significant clay mass at silt diameters argues that the original soil size distribution subject to wind erosion is significantly dispersed by wet sieving. The alternation of carbonates and their distribution with respect to size during emission (Caquineau et al., 1998) suggests that they too are modified during the soil analyses used to construct the MMT. An important challenge for modeling the aerosol size distribution is thus to reconstruct the undispersed size distribution of the soil. A related challenge is to represent the modification of this size distribution as soil particles are mobilized and converted into aerosols. Direct entrainment by the wind of the smaller dust particles that travel thousands of kilometers downwind from their source (whose diameters are generally below 20 µm) is small due to the strong cohesive forces binding soil particles into aggregates of larger sizes (Iversen et al., 1976). Paradoxically, larger and heavier soil grains or aggregates are more easily lifted because their cohesive forces are small (Iversen and White, 1982). Most of the smaller particles that are dispersed globally are entrained into the atmosphere during the fragmentation of clay and silt aggregates, either by saltation bombardment by larger sand-sized particles (with diameters between 50 and 2000 µm) or the fragmentation of aggregates large enough to be lifted directly by the wind (Shao et al., 1993; Kok, 2011; Marticorena, 2014). Frag-

ACPD
15, 3493–3575, 2015

mentation is an important source of clay-sized aerosols, although the abundance of phyllosilicate mass at silt sizes in Fig. 1 makes it clear that many soil aggregates are not broken into clay-sized aerosols during mobilization.

An additional modeling challenge is that different minerals may have different size distributions in the soil and may not be equally susceptible to disaggregation and fragmentation during wet sieving and emission, respectively. The size distribution of each mineral in Fig. 1 is normalized with respect to its total volume, allowing comparison of the characteristic particle size between different minerals. For example, Fig. 1 shows that a greater fraction of quartz mass is found at large particle sizes, compared to other minerals. Differences in the aerosol size distribution among minerals may result from contrasting size distributions in the parent soil as well as different aggregation and fragmentation properties of each mineral. A model must account for these contrasts to reproduce observations that far-travelled aerosols are depleted in quartz compared to the fraction of this mineral in the parent soil (Glaccum and Prospero, 1980; Jeong, 2008).

In Sect. 2.2, we describe a method to calculate the mineral composition of soil dust aerosols. We begin by calculating regional variations in the soil mineral content following Claquin et al. (1999), through a combination of an MMT and a global atlas of soil texture. We propose two extensions to address assumptions noted by that study. First, we describe a semi-empirical method to reconstruct the undispersed size distribution of soil particles, prior to the wet sieving, and its modification during emission. This extension is described in more detail in Sect. 2.1.2.

Our second extension is to account for mixtures of different minerals. Individual particles comprising soil dust aerosols are often observed as mixtures of distinct minerals (Kandler et al., 2011; Scheuvens and Kandler, 2014; Jeong and Nousiainen, 2014), whose representation imposes a potentially large computational burden. For example, the number of combinations consisting solely of mineral pairs increases geometrically with the number of represented minerals.

ACPD
15, 3493–3575, 2015

For minerals removed from the atmosphere at the same rate, their combination can be represented as an external mixture, requiring no additional prognostic variables. The rate of aerosol removal is distinguished in part by particle density that controls the speed of gravitational settling. Many minerals commonly observed to comprise dust particles have similar densities, suggesting that external mixing is a reasonable idealization that is attractive for its computational simplicity. (As a caveat, we note that particles of similar density that experience similar rates of gravitational settling may nonetheless be differentiated during wet deposition through contrasts in mineral solubility. We neglect this complexity in the present study.)

Iron oxides, like hematite and goethite, are an exception. Their density is twice that of the other minerals, and would thus be removed by gravitational settling within roughly half the distance from their source. However, iron oxides can exist as small impurities that are internally mixed with other minerals (Kandler et al., 2007; Scheuvens et al., 2011). These accretions are only a small fraction of the total particle mass, and only slightly perturb the particle density that is determined primarily by the density of the host mineral. Iron oxides present as a small impurity will travel farther than in their pure crystalline form.

To our knowlege, measurements of mineral mixtures within individual aerosol particles are mostly anecdotal and provide only limited guidance about the combinations that need to be represented by a global model. In this study, the only combinations we represent explicitly are internal mixtures of iron oxides with another mineral, following Balkanski et al. (2007) and Scanza et al. (2015). This assumes that the former is present in small enough concentration to make a negligible perturbation to the particle density. Our construction of mixtures is described in Sect. 2.2.2. Previous treatments of aerosol mineral content have addressed the role of clays and feldspars as ice nuclei (e.g. Hoose et al., 2008; Atkinson et al., 2013), circumventing the consideration of iron oxide transport and mineral combinations. Our treatment of iron oxide impurities is possibly more speculative and subject to revision than the remainder of our method. Nonetheless, we address their transport because of their importance for shortwave

ACPD
15, 3493–3575, 2015

absorption and deposition of bioavailable iron, even though we don't consider these applications in this study.

Our extensions to Claquin et al. (1999) are semi-empirical and based upon limited size-resolved measurements of aerosol minerals. Ultimately, we hope that our semi-empirical approach will be made unnecessary by routine measurements of undispersed soil particle size and a more physically based model of emission. In the meantime, we illustrate the validity of our approach by comparison to an extensive global compilation of measurements, as described in Part 2 of this article (Perlwitz et al., 2015) and in Pérez García-Pando et al. (2015).

2.1.2 Observational constraints upon the emitted size distribution

The transformation of the particle size distribution of the (undispersed) parent soil into the emitted size distribution is a complicated process that depends upon wind speed and the physical properties of the soil and land surface (Shao, 2001; Alfaro and Gomes, 2001; Grini et al., 2002; Marticorena, 2014). However, measurements suggest that for the smallest particles (including the far-travelled particles that are transported globally), the size distribution is approximately invariant, independent of wind speed and soil properties (Gillette et al., 1972, 1974; Gillette, 1974; Sow et al., 2009). The theory of brittle fragmentation suggests that this is likely a robust result, despite the limited measurements of size-resolved emission (Kok, 2011). We will use this approximate invariance to calculate the emitted size distribution, after reconstructing the distribution of the original, undispersed soil.

Kok (2011) provides a theory for the emitted volume as a function of particle diameter D that begins with the size distribution for a soil that is fully dispersed, for example, by wet sieving. First, the size distribution of the undispersed soil, $u(D)$ is approximately reconstructed using a method proposed by Shao (2001), who assumes that the number of reconstructed aggregates with diameter D is proportional to the fraction of wet-sieved particles smaller than D. The qualitative effect of this method is to redistribute the smallest particles in the wet-sieved soil toward larger sized aggregates in the orig-

ACPD
15, 3493–3575, 2015

inal soil (cf. Fig. 4 of Shao, 2001). Next, the modification during emission of the size distribution of the original soil is calculated assuming brittle fragmentation. This process is assumed to control the emitted size distribution for particle diameters less than roughly 20 µm. (Above this diameter, variations in wind speed are expected to have influence.) Within this range, the size distribution of the emitted dust volume (V) is:

$$\frac{dV}{d\ln D} = \frac{D}{C_V} u(D) \exp\left[-\left(\frac{D}{\lambda}\right)^3\right] \quad (1)$$

where C_V is a normalization factor. The exponential on the right side of Eq. (1) represents the fragmentation of aggregates during emission. The length scale $\lambda = 12 \pm 1$ µm was obtained by Kok (2011), who performed a least-squares fit to the few available measurements of the emitted size distribution (Gillette et al., 1972, 1974; Gillette, 1974; Sow et al., 2009), after estimating $u(D)$ from measured size distributions of arid dispersed soils (d'Almeida and Schütz, 1983; Goldstein et al., 2005). The derived value of λ is roughly ten percent of a typical aggregate diameter (cf. Fig. 1), consistent with the assumption that the emitted particles are created by the fracture of aggregrates.

The normalized distribution of emitted volume is shown as a black line in Fig. 2, derived from the corresponding distribution of the fully dispersed soil shown in orange. In this example, the ratio of clay-sized mass to silt is 0.5 in the fully dispersed soil but only 0.05 after emission of the undispersed soil. (The silt fraction here represents the sum of particle diameters up to 20 µm, below which we assume Eq. 1 is applicable.) The redistribution of emitted mass away from clay sizes compared to the fully dispersed soil (the black and orange curves in Fig. 2, respectively) shows that fragmentation of aggregates during emission results in fewer clay-sized particles than breaking of aggregates during dispersion of the soil prior to measurement. The net effect of reconstruction of the undispersed soil combined with fragmentation during emission is to increase the silt-sized fraction at the expense of clay. The dotted curve in Fig. 2 shows the contribution to silt emission from clay-sized particles in the fully dispersed soil. This contribution corresponds to about 45 % of the emitted silt mass. This redistribution is consistent with

ACPD
15, 3493–3575, 2015

measured size distributions of concentration, including the nomimal "clay" minerals like phyllosilicates in Fig. 1, whose mass abundance is largest at silt sizes.

We will follow Claquin et al. (1999) to calculate regional variations in the mineral fractions of the dispersed soil, but augment the emitted silt fraction with clay-sized minerals. For example, we assume that phyllosilicates in the parent soil are also emitted at silt sizes even though these minerals are present in the MMT for the fully dispersed soil only at clay sizes (Claquin et al., 1999). This augmentation crudely represents reconstruction of the original size distribution of the undispersed soil modified by brittle fragmentation during emission (represented by the dotted curve in Fig. 2). We will also use Eq. (1), the emitted size distribution derived by Kok (2011), to specify the relative fraction of emitted clay and silt-sized particles. The prescription of an emitted size distribution that is independent of location is shared by studies of the global dust cycle that do not resolve mineral variations (e.g. Miller et al., 2006; Albani et al., 2014). This approach has also been used by Scanza et al. (2015) to account for the effects of reaggregation and fragmentation upon the aerosol mineral composition.

The process of brittle fragmentation that leads to the emitted size distribution in Fig. 2 is expected to be valid for diameters on the order of λ, beyond which the size distribution evolves through sandblasting with a complicated dependence upon wind speed and soil properties (Kok, 2011). We assume that the specific range of validity extends to 20 µm. This upper bound is mismatched with respect to the MMT whose silt size category extends to particle diameters up to 50 µm. To constrain the fraction of clay and silt-sized particles over the size range corresponding to the MMT, we need to know the size distribution between 20 and 50 µm. We specify this with the concentration measurements in Fig. 3 (left panel) from the SAMUM campaign in Morocco (Kandler et al., 2009). (This figure is identical to Fig. 1, but is summed over all minerals and renormalized between 0 and 50 µm, the range of particle diameters corresponding to the MMT.) This figure provides the mass ratio corresponding to particle diameters between 2 to 20 µm compared to diameters between 20 to 50 µm. Combining this ratio with the fraction of clay to silt particles with diameters up to 20 µm provided by Eq. (1), equal

ACPD
15, 3493–3575, 2015

to 0.05, we calculate that clay particles contribute 1.3 % of the total emitted mass for particle diameters up to 50 µm. By combining the size distributions of Kok (2011) and Kandler et al. (2009) in their regions of respective validity, we arrive at the "corrected" size distribution shown in the second panel from the left in Fig. 3.

By constraining emission with concentration measurements at a single location, we are making at least two approximations. First, we are neglecting modification to the emitted size distribution by deposition that preferentially removes larger particles by gravitational settling. We partially account for this removal by using concentration measured only during high-dust events (Fig. 1, bottom row), which we assume correspond to recent emission. (We interpret the presence of large particles with diameters over 100 µm as evidence that deposition has had little time to modify the emitted distribution.) Second, we assume that the emitted size distribution of each mineral depends primarily upon the mineral's intrinsic physical characterisitics including its tendency to fragment, neglecting a dependence upon wind speed and soil properties that will cause the distribution to vary with location. This neglect is less defensible for diameters between 20 and 50 µm (compared to smaller particles for which Eq. (1) is a good approximation), but quantifying the validity of our assumption would require an emission model whose complexity is beyond the goals of the present study.

2.2 Calculating mineral fractions at emission

2.2.1 Algorithm

Here, we describe our calculation of the emitted fraction of each mineral and its particle size distribution. We treat the dust particles as an external mixture of minerals, each corresponding to a separate prognostic variable. We create additional prognostic variables for mixtures of each mineral with iron oxides, where the latter is assumed to be a small fraction of the total particle mass. Calculation of iron oxide mixtures is described separately in Sect. 2.2.2.

ACPD
15, 3493–3575, 2015

We first derive the mineral composition of the fully dispersed soil following Claquin et al. (1999). Their MMT gives $f_n^c(a)$ and $f_n^s(a)$, the mass fraction of mineral n in the clay (0 to 2 µm) and silt (2 to 50 µm) size categories, respectively, as a function of a, the arid soil type, whose spatial distribution is provided by the DSMW (FAO, 2007) that is integrated into the Harmonized World Soil Database (HWSD FAO/IIASA/ISRIC/ISSCAS/JRC, 2012). (Table 1 describes the data sets used in this study.) For each value of soil type a (that implicitly varies with location), the mineral fractions given by the MMT sum to unity:

$$\sum_n^N f_n^c(a) = 1 \text{ and } \sum_n^N f_n^s(a) = 1, \quad (2)$$

For Claquin et al. (1999), only calcite (or more generally, "carbonates") and quartz are present at all particle sizes. Phyllosilicates (illite, kaolinite, smectite) are present only at clay sizes, while feldspar, gypsum and hematite are restricted to silt sizes. Based upon measurements shown in Fig. 1, we assume that each mineral is present within all size categories, so that N, the total number of minerals, equals 8 for both clay and silt-sized particles (Table 2). The iron oxide fraction provided by the MMT was originally derived using soil redness and assigned to the silt size category without reference to its measured size distribution. However, soil measurements show that iron oxides are present over a range of diameters as small as nanometers (Shi et al., 2012). Following Nickovic et al. (2012), we assume that iron oxide is present at both clay and silt sizes, assuming that the clay fraction is identical to the silt fraction provided by the MMT. We assume that the iron oxide fraction that is newly introduced at clay sizes occurs at the expense of the phyllosilicate fractions within the MMT. This is partly because iron oxides are a weathering product of phyllosilicates, but in practice this offset causes only a small reduction of the phyllosilicate fraction. The extension of the feldspar and gypsum MMT mineral fractions to clay sizes is described below.

To calculate the mineral fractions of the dispersed soil at each location, we specify the fraction of each size category present, provided by the soil texture class b, whose

ACPD
15, 3493–3575, 2015

spatial distribution is provided by the FAO/STATSGO soil texture (Table 1). Let $s^c(b)$ and $s^s(b)$ be the mass fractions of clay and silt-sized particles provided by the soil texture triangle for each soil texture class b (Table 3). The clay and silt-size fractions are normalized to sum to unity at each location:

$$s^c(b) + s^s(b) = 1. \quad (3)$$

Thus, the soil mass fraction of each mineral in the clay and silt-size categories, s_n^c and s_n^s, respectively, is given by:

$$s_n^c(a,b) = s^c(b) f_n^c(a) \text{ and } s_n^s(a,b) = s^s(b) f_n^s(a) \quad (4)$$

As a result of Eqs. (2) and (3), the soil mass fractions sum to unity:

$$\sum_n^N \left(s_n^c + s_n^s\right) = 1. \quad (5)$$

The soil mass fraction of each mineral varies regionally through its dependence upon the arid soil type a (through the MMT that gives the fractional mineral composition of each size category) and soil texture b (that gives the local fractional abundance of each size category). For brevity, we will hereafter omit the dependence of s_n^c and s_n^s upon a and b (and implicitly upon location).

We have derived Eq. (4), the mass fraction of each mineral within the dispersed soil, by applying the method of Claquin et al. (1999) with the extension of hematite to clay sizes following Nickovic et al. (2012). What remains is to specify the *emitted* fraction of each mineral within each size category.

Let d^c and d^s be the mass fractions of emitted clay and silt-sized aerosols, respectively, that at each location satisfy:

$$d^c + d^s = 1. \quad (6)$$

ACPD
15, 3493–3575, 2015

We further decompose each aerosol mass fraction into contributions from the N minerals. Let d_n^c and d_n^s represent the contribution of mineral n to mass fraction of emitted clay and silt-sized particles, respectively:

$$d^c = \sum_n^N d_n^c \text{ and } d^s = \sum_n^N d_n^s, \tag{7}$$

that because of Eq. (6) satisfy:

$$\sum_n^N \left(d_n^c + d_n^s\right) = 1. \tag{8}$$

As a simple way to account for dispersion in the soil texture measurements and MMT, along with the fragmentation of aggregates during emission, we prescribe the mass fraction of emitted clay-sized particles, as described in Sect. 2.1.2 and shown in Fig. 3 (second panel from the left):

$$d^c = 0.013. \tag{9}$$

We assume that d^c is independent of location, based upon Kok (2011), who argues that the black curve in Fig. 2 is a good approximation to measurements of the emitted size fraction for a variety of soils and wind conditions. Because of Eq. (6), the emitted silt fraction d^s is implicitly determined:

$$d^s = 1 - d^c = 0.987. \tag{10}$$

Our second assumption is that the emitted silt fraction d^s is a combination of silt-sized particles in the dispersed soil along with aggregates in the original soil that were dispersed into clay-sized particles during wet sieving. We represent this restoration of aggregates empirically by augmenting emission at silt sizes in proportion to the fractional abundance of clay particles (s_n^c) in the fully dispersed soil:

$$d_n^s = \eta(\gamma_n s_n^c + s_n^s). \tag{11}$$

ACPD
15, 3493–3575, 2015

Here, γ_n is a coefficient of proportionality that controls the magnitude of augmentation. For simplicity, we assume that γ_n is identical for all reaggregated minerals, except for feldspar and gypsum, which are treated separately as described below. The remaining exception is quartz, whose abundance at large diameters in Fig. 1 suggests that it experiences minimal dispersion, which we represent approximately by setting $\gamma_n = 0$. The parameter η is calculated at each location to satisfy Eq. (10).

As a consequence of Eqs. (4) and (9), the emission of clay-sized mineral n (excluding feldspar and gypsum) is:

$$d_n^{\mathrm{c}}(a) = d^{\mathrm{c}} f_n^{\mathrm{c}}(a) \quad \text{where } d^{\mathrm{c}} = 0.013. \tag{12}$$

Note that reaggregation is assumed to have no effect upon the proportions of minerals emitted at clay sizes, which are thus identical to the soil mineral fractions given by Eq. (4), aside from a multiplicative constant.

Similarly, the emitted silt fraction of mineral n is:

$$d_n^{\mathrm{s}}(a,b) = \eta(a,b)\left[\gamma_n s^{\mathrm{c}}(b) f_n^{\mathrm{c}}(a) + s^{\mathrm{s}}(b) f_n^{\mathrm{s}}(a)\right], \tag{13}$$

noting that $\gamma_n \equiv \gamma$, an identical constant all minerals, except for quartz, for which $\gamma_n \equiv 0$. We have temporarily noted the dependence of the silt fraction d^{s} upon the local soil type a and texture b.

Equation 13 extends clay-sized minerals like phyllosilicates into the silt-size range, consistent with measurements by Kandler et al. (2009) in Fig. 1. Because the total fractional silt emission is assumed to be fixed according to (10), γ has the effect of reducing the fractional emission of minerals like quartz that are predominately silt-sized in the dispersed soil. We show below and in Part 2 (Perlwitz et al., 2015) that this reduction leads to improved agreement with observations. This fractional reduction of emitted minerals whose size is largely unmodified by wet sieving is a consequence of the reintroduction of aggregates reconstructed from clay-sized minerals that were originally created by dispersion.

ACPD
15, 3493–3575, 2015

To extend feldspar and gypsum emission into clay sizes (motivated by Fig. 1), we start with the mass ratio of clay-sized particles compared to silt particles with diameters less than 20 µm, equal to 0.05, according to Fig. 2 that is based upon (Kok, 2011). For each mineral, we then use the concentration ratio measured during SAMUM of particle diameter from 2 to 20 µm and 20 to 50 µm (based upon the mass distributions shown in the right two panels of Fig. 3). This gives:

$$d_n^{\mathrm{c}} = \alpha_n d_n^{\mathrm{s}} \tag{14}$$

where:

$$d_n^{\mathrm{s}} = \eta(a,b)s^{\mathrm{s}}(b)f_n^{\mathrm{s}}(a) \tag{15}$$

where n corresponds to feldspar and gypsum. Due to the a posteriori extension of feldspar and gypsum into clay sizes, we proportionally reduce the fractions of illite, smectite and kaolinite in the fraction of clay-sized dust. Note that the derivation of Eq. (14) is identical to the derivation of $d^{\mathrm{c}} = 0.013$, except that the latter uses the measured size distribution summed over all minerals (Fig. 2, left panel), while the derivation of α_n is based upon the size distribution of either feldspar or gypsum (Fig. 3, right panels).

The emitted silt particles have diameters ranging between 2 and 50 µm (consistent with the MMT). We distribute each mineral's silt particles over the size categories transported by ModelE (Table 4). (Clay-sized particles are transported in a single bin by ModelE, so distribution within this size range is unnecessary.) We introduce an additional model size category between 32 and 50 µm that is not transported so that the total silt size range within the model and MMT are identical. Let $d_{n,k}^{\mathrm{s}}$ be the emitted mass fraction of mineral n within size category k. To distribute the silt mass, we use the normalized mass distribution of each mineral derived from measurements of surface concentration during SAMUM (Kandler et al., 2009), shown in Fig. 4. We define $m_{n,k}^{\mathrm{s}}$ as the mass fraction within size bin k that is normalized for each mineral n over

ACPD
15, 3493–3575, 2015

the MMT silt range (between 2 and 50 µm) so that:

$$\sum_{k \in \substack{\text{all silt} \\ \text{size bins}}} m^{s}_{n,k} = 1 \text{ for each mineral } n. \quad (16)$$

Then, the emitted silt within each size bin k is:

$$d^{s}_{n,k} = d^{s}_{n} m^{s}_{n,k} \quad (17)$$

(The $m^{s}_{n,k}$ are proportional to the values shown in Fig. 4, but differ because the former are normalized only over the range of silt sizes. In contrast, the values in Fig. 4 include the clay-size bin in their normalization.)

Finally, we renormalize the mass fractions d^{c}_{n} and $d^{s}_{n,k}$ so that their sum over all minerals and sizes is unity for diameters up to 32 µm. (Silt particles with diameters between 32 and 50 µm are not transported by the model.) This renormalization has the effect of reducing the fraction of quartz fraction compared to the MMT. This is because a greater mass fraction of quartz is measured at diameters above 32 µm, compared to other minerals, according to Fig. 4. For example, quartz has 38 % of its mass between 32 and 50 µm, a significantly larger amount than that of carbonates (23 %), feldspar (30 %) and particularly gypsum (2 %). The shift of quartz aerosols toward larger diameters compared of other minerals results from the larger characteristic particle size of quartz in the parent soil. Thus, the fractional emission of quartz at silt sizes is reduced by two effects compared to the fraction indicated by the MMT: the reaggregation of clay-sized particles and the limited size range of our transport model. The second effect is simply the result of a disproportionate mass of quartz at diameters that are too large to travel far from their source.

Our model generally resembles that of Scanza et al. (2015) although there are differences that illuminate the physical processes represented by both studies. Our method of reaggregation Eq. (13) accounts for local soil texture, reconstructing more aggregates where s_c, the fraction of clay-sized particles, is particularly large. In contrast,

ACPD
15, 3493–3575, 2015

Scanza et al. (2015) assume a globally invariant size distribution of the wet-sieved soil. In addition, the latter study reconstructs the aggregates of all minerals identically, including quartz, whose reaggregation we neglect due to its presumed mechanical stability and resistance to distinegration during wet sieving. This neglect reduces the relative fraction of quartz at silt sizes in our model. Finally, we use the measurements of Kandler et al. (2009) to account for the disparity between the size range appropriate for brittle fragmentation theory (diameters less than roughly 20 µm) and the MMT (diameters less than roughly 50 µm). In contrast, Scanza et al. (2015) use the entire silt fraction of quartz assigned by the MMT that includes diameters above 20 µm where brittle fragmentation theory is not directly applicable. This contrast further reduces the relative fraction of quartz in our model, because a disproportionate amount of quartz given by the MMT is at these larger sizes.

2.2.2 Transport of iron oxides as internal mixtures

In our model, iron oxides can travel either in pure crystalline form or as an internal mixture with other minerals. (Combinations of the other minerals excluding iron oxides are treated as external mixtures.) Our apportionment of iron oxides combines the two limiting cases considered by Scanza et al. (2015). In that study, iron oxide is treated either a pure component within an external mixture, or else an internal mixture with phyllosilicates and the other minerals.

At each location, Eqs. (12) and (13), along with (14) and (15), give us $d^{c}_{n,k}$ and $d^{s}_{n,k}$, including the mass fraction of emitted iron oxide. To create mixtures with other minerals, we will specify the hematite fraction available for mixing along with its mass fraction in each particle. (We describe mixtures in terms of "iron oxides" rather than hematite, whose fraction is provided by the MMT, because our mixing method applies to other highly weathered iron minerals like goethite that are frequently found in aggregation (Lafon et al., 2006; Kandler et al., 2007).)

To simplify notation, we drop the superscripts in Eqs. (12), (13), (14) and (15) that distinguish between clay and silt-sized particles, and denote particle size solely through

ACPD
15, 3493–3575, 2015

the k index of $d_{n,k}$. For the GISS ModelE, $k = 1$ corresponds to the clay-sized fraction, while transported silt sizes correspond to k equal 2 through 5 (Table 4).

We first distinguish between each mineral in its pure and mixed state:

$$d_{n,k} = d_{n,k}^{\text{pure}} + d_{n,k}^{\text{mix}}. \tag{18}$$

For the particular case of iron oxides, we replace the mineral index n with Fe, so that $d_{\text{Fe},k}$ denotes the emitted mass fraction of iron oxide in size category k. Then, analogous to Eq. (18), iron oxides can be decomposed into pure crystals and impurities mixed with other minerals:

$$d_{\text{Fe},k} = d_{\text{Fe},k}^{\text{pure}} + d_{\text{Fe},k}^{\text{mix}}. \tag{19}$$

We further distinguish the mixture of iron oxide among the remaining minerals as $d_{\text{Fe}|n,k}^{\text{mix}}$, so that the total iron oxide within mixtures is the sum over n:

$$d_{\text{Fe},k}^{\text{mix}} = \sum_{n \neq \text{iron oxide}} d_{\text{Fe}|n,k}^{\text{mix}}. \tag{20}$$

We determine $d_{\text{Fe}|n,k}^{\text{mix}}$ by first specifying the fraction of emitted iron oxide available for mixing. Define ϵ as the fraction of emitted iron oxide transported as pure crystals:

$$d_{\text{Fe},k}^{\text{pure}} = \epsilon d_{\text{Fe},k}, \tag{21}$$

We assume that ϵ itself is proportional to the total iron oxide:

$$\epsilon = \epsilon_0 d_{\text{Fe},k}. \tag{22}$$

Then:

$$d_{\text{Fe},k}^{\text{pure}} = \epsilon_0 d_{\text{Fe},k}^2, \tag{23}$$

ACPD
15, 3493–3575, 2015

and using Eq. (19):

$$d^{\text{mix}}_{\text{Fe},k} = (1-\epsilon)d_{\text{Fe},k} = (1-\epsilon_0 d_{\text{Fe},k})d_{\text{Fe},k}. \quad (24)$$

Equation (22) expresses our assumption that the fraction of pure crystalline iron oxide increases where the total iron oxide fraction is large, a heuristic attempt to account for the weathering that creates iron oxides in the soil. As soil develops, more of the primary and secondary Fe-bearing minerals decompose and the iron of their lattice structure is converted to iron oxides in the soil (McFadden and Hendricks, 1985; Shi et al., 2012). Micrometer-sized crystalline iron oxide aggregates are typically observed in highly weathered soils that are rich in iron oxides (Chesworth, 2008). Therefore, we assume that the amount of crystalline iron oxides not attached as small impurities to other minerals is proportional to the total iron oxide content of the soil. In absence of quantitative observational constraints, we simply set $\epsilon_0 = 1$. In the future, ϵ_0 could be prescribed differently or even be a function of other soil properties.

We next assume that iron oxide is mixed with the other minerals in proportion R to the total particle mass:

$$d^{\text{mix}}_{\text{Fe}|n,k} = R\left(d^{\text{mix}}_{n,k} + d^{\text{mix}}_{\text{Fe}|n,k}\right). \quad (25)$$

We assume that R is a small number so that the iron oxides only slightly perturb the density of the mixture. We are aware of few measurements that guide a more precise choice of this parameter. We set R equal to 0.05, and calculate in Sect. 4.4 that the contribution of aggregated iron oxide to the global dust load is just under 2 %, comparable with the fraction inferred or assumed by other studies (e.g. Sokolik and Toon, 1999; Koven and Fung, 2006; Balkanski et al., 2007; Wagner et al., 2012; Moosmüller et al., 2012). In that section, we suggest that this global fraction is insensitive to our choice of R.

ACPD
15, 3493–3575, 2015

Finally, we assume that the iron oxide available for mixing is distributed among the other minerals in proportion to their mass fraction:

$$d^{\text{mix}}_{\text{Fe}|n,k} \propto \frac{d_{n,k}}{\overline{d}_k} \tag{26}$$

where $\overline{d}_k$ is the mass fraction for each size category summed over all minerals except for iron oxide.

$$\overline{d}_k = \sum_{n \neq \text{iron oxide}} d_{n,k} \tag{27}$$

Equation (26) is a reasonable first assumption, although future efforts might construct mixtures by considering whether iron oxides are more likely to be created by weathering of specific minerals. For example, iron oxides and clay minerals are formed during chemical weathering of parent minerals and are in intimate physical association with each other (Reid et al., 2003; Shi et al., 2012). As a result of Eqs. (24) and (26):

$$d^{\text{mix}}_{\text{Fe}|n,k} = \left(1 - d_{\text{Fe},k}\right) d_{\text{Fe},k} \frac{d_{n,k}}{\overline{d}_k} \tag{28}$$

In an appendix, we use these assumptions to derive the emitted mass fraction of iron oxide mixed with mineral n:

$$d^{\text{mix}}_{n,k} + d^{\text{mix}}_{\text{Fe}|n,k} = \min\left[\frac{\left(1 - d_{\text{Fe},k}\right) d_{\text{Fe},k}}{R} \frac{d_{n,k}}{\overline{d}_k}, \frac{d_{n,k}}{1 - R}\right]. \tag{29}$$

As shown in the appendix, the second term within the minimum results from the possibility that for small enough mass fractions of accreted iron oxide within each particle ($R \ll 1$), there will be insufficient amounts of mineral n available for combination with the amount of iron oxide specified by Eq. (24).

ACPD
15, 3493–3575, 2015

The mass fraction of pure, crystalline iron oxide is given by:

$$d_{\mathrm{Fe},k}^{\mathrm{pure}} = d_{\mathrm{Fe},k} - \min\left[(1 - d_{\mathrm{Fe},k})d_{\mathrm{Fe},k}, \frac{R}{1-R}\overline{d}_k\right], \tag{30}$$

while the mass fraction of pure mineral n is given by:

$$d_{n,k}^{\mathrm{pure}} = d_{n,k} - \left(\frac{1-R}{R}\right) d_{\mathrm{Fe}|n,k}^{\mathrm{mix}}. \tag{31}$$

According to Eq. (29), iron oxide is accreted with a host mineral within the same size category k. For example, silt-sized mixtures are formed from iron oxide mass in the same size category. This might seem inconsistent, because the accreted iron oxide is assumed to be only a small fraction R of the total particle mass. However, the silt fraction of each mineral measured by Kandler et al. (2009) is the mass fraction within the total *collection of* particles of silt size, and not the fraction of iron oxide particles at this size. That is, at least some of the measured iron oxide mass at silt sizes consists of smaller crystals of this mineral attached to host minerals with silt diameters, as shown by images of single particles (Scheuvens and Kandler, 2014). Our modeling assumptions leading to Eq. (29) should be evaluated with more measurements of the size distribution and mixing state of iron oxides in the soil.

2.3 Soil dust tracers in ModelE

Our model of the emitted mineral fractions has been incorporated into the AR5 version of the NASA GISS Earth System ModelE2 (Schmidt et al., 2014) that has horizontal resolution of 2° latitude by 2.5° longitude and 40 vertical layers up to 0.1 hPa. Here, we summarize the dust aerosol module that is largely unchanged since its description in Miller et al. (2006). The values $d_{n,k}$ give the fractional emission of each mineral. What remains is to calculate the absolute value of emission at each location.

Emission occurs when the surface wind speed w exceeds a threshold w_T. Subgrid variations of w are introduced using a probability distribution $p(w)\,\mathrm{d}w$ (Cakmur et al.,

ACPD
15, 3493–3575, 2015

2004), so that the total emission E at each location is:

$$E = CSZ \int_{w_T}^{\infty} w^2 (w - w_T)\, p(w)\, \mathrm{d}w, \tag{32}$$

where S identifies regions of abundant easily erodible soil particles, and is an updated version of the source map derived by Ginoux et al. (2001). The parameter Z identifies regions of sparse vegetation, where the soil particles are exposed to the force of the wind, and is derived from the climatological annual cycle of surface roughness retrieved from a microwave scatterometer (Prigent et al., 2005). The threshold wind speed w_T in Eq. (32) increases with soil wetness q, following Shao et al. (1996):

$$w_T = w_{T,0} \exp(0.7q), \tag{33}$$

where $w_{T,0} = 8\,\mathrm{m\ s^{-1}}$ is the emission threshold of the 10 m surface wind speed for completely dry soil. The value C controls the magnitude of the global dust cycle, and in the present case is chosen to give global, annual emission for all experiments of 2224 ± 100 Tg for particle diameters up to 32 µm (Table 7). This is within the range of values calculated by recent global models (Huneeus et al., 2011), and remains the case even if our model emission is restricted to smaller diameters (up to 16 µm) that are dispersed farther downwind of their source. Our model evaluation is independent of global emission because the observations consist of mineral fractions (Perlwitz et al., 2015).

Emission of each mineral is the total emission E from Eq. (32) multiplied by the fractions $d_{n,k}$ (and their decompostion into pure and mixed states) derived above.

Each mineral is advected using the Quadratic Upstream Scheme (Prather, 1986), which keeps track of nine subgrid-scale moments as well as the tracer mean within each grid box, increasing the effective resolution for transport.

Removal of the mineral tracers from the atmosphere takes place by wet and dry deposition. Dry deposition includes gravitational settling and turbulent deposition in the

ACPD
15, 3493–3575, 2015

surface layer. Settling speeds are proportional to mineral density (Tegen and Fung, 1994), whose values are given in Table 8. Note that the minerals have nearly identical densities, except for iron oxides whose density is nearly twice the value of the other minerals. Turbulent mixing near the surface is calculated using the same exchange coefficient as humidity. The calculations of the deposition velocities in the surface layer are based on a "resistance in series" scheme (Wesely and Hicks, 1977; Koch et al., 1999).

Wet deposition occurs through scavenging both within and below clouds where there is precipitating condensate. Within clouds, dust aerosols are scavenged where they nucleate precipitating cloud droplets. Dust particles are assumed to be 50 % soluble. This scheme is used for the other aerosol species within ModelE2 (Koch et al., 1999), and is more mechanistically based than the single scavenging coefficient used by Miller et al. (2006).

3 Model simulations

We evaluate our new approach in comparison to a baseline simulation that assumes the emitted mineral fractions are identical to those of the wet-sieved soil. We conduct a set of simulations with the NASA GISS ModelE covering the years 2002 to 2010. This period coincides with a period of detailed measurements at Izaña (Rodríguez et al., 2011), and includes many of the measurements from our global compilation listed in the companion article (Perlwitz et al., 2015). We relax the model winds at each level every six hours toward their NCEP reanalysis values, in an effort to reproduce the observed transport. We also prescribe sea surface temperature and sea ice based upon measurements (Rayner et al., 2003). The prognostic mineral aerosols are assumed to have no radiative effect in the present study. Instead dust radiative forcing is prescribed from a climatological distribution of dust aerosols whose radiative properties are assumed to be regionally invariant (Miller et al., 2006). This eliminates any feed-

ACPD
15, 3493–3575, 2015

back between radiative forcing by the mineral aerosols and their emission resulting, for example, from the perturbed surface wind speed.

Our baseline simulation is referred to as the "soil mineral fraction" (SMF) method, and assumes that the emitted mineral fractions are identical to those of the wet-sieved soil, given by Eq. (4). The wet-sieved soil fractions are derived using the MMT of Claquin et al. (1999), augmented by mineral fractions for three additional soil types provided by Nickovic et al. (2012). Following this later study, iron oxides are extended into the clay-sized category using MMT fractions identical to their values for silt sizes. The emitted silt-sized minerals are distributed over the ModelE size bins according to Eq. (17), whose mass fractions are derived from concentration measurements at Tinfou, Morocco (Kandler et al., 2009). The ratio of emitted clay to silt in the SMF experiment is given by the local soil texture.

Our new approach, hereafter described as the "aerosol mineral fraction" (AMF) method, is described in Sect. 2.2. The emitted mineral fractions are based upon the MMT soil mineral fractions Eq. (4), modified to account for disaggregation during wet-sieving and fragmentation during emission. The AMF method extends feldspar and gypsum into the clay fraction using Eqs. (14) and (15). For the other minerals, clay-sized emission derives from Eq. (12); silt-sized emission is taken from Eq. (13), with its allocation into the ModelE silt-size bins according to Eq. (17). Mixtures of iron oxides with other minerals are estimated according to Eqs. (29)–(31).

The AMF simulation sets our empirical reaggregation parameter γ equal to 2. We performed a simulation with $\gamma = 3.5$ to examine the sensitivity of our results to enhanced reaggregation. In addition, we set $\gamma = 0$ in one experiment to illuminate the physical origin of differences between the AMF and SMF methods. The experiment with $\gamma = 0$ uses an emitted size distribution consistent with measurements and the default AMF experiment, but resembles the SMF method by not reconstructing silt-sized aggregates to undo the effect of wet sieving.

We carried out two more experiments to show the effect of different treatments of iron oxides. The first is the AMF experiment but without accretions of iron oxides within other

ACPD
15, 3493–3575, 2015

minerals (denoted by "AMF-NoFeAcc"). The second (denoted as "SMF-NoClayFe") corresponds to the SMF experiment, but without the extension of iron oxides into clay sizes proposed by Nickovic et al. (2012). Our simulations are summarized in Table 9.

4 Results

4.1 Emitted size distribution and implications for long-range transport

We first compare the emitted distributions of dust particles, summed over all minerals and derived from the AMF and SMF experiments along with their impact upon long-range transport. This analysis helps to understand regional variations of surface concentration for each mineral, presented in Sect. 4.3.

Figure 5 displays the emitted mass for each ModelE size bin calculated using the SMF and AMF methods. For each SMF size bin, emission varies according to the local soil texture. For the AMF method, the size distribution varies additionally due to reaggregation of certain clay-sized minerals. For each size bin, we calculate the distribution of the emitted fraction of each mineral with respect to the 336 combinations of the twelve soil texture categories along with the twenty-eight DSMW soil types included in the MMT. The emitted fractions are weighted by the total emission (at all sizes) to emphasize prolific sources. The median emission is marked in the figure by a crossbar with variability indicated by other parameters identified in the caption. Each combination of soil type and texture is characterized at the native resolution of the DSMW ($5' \times 5'$ latitude by longitude). For each grid box, emission is normalized so that the sum across all sizes (up to 50 µm diameter) is unity, which emphasizes the particle size making the largest contribution to emission. (In the model, normalization extends only to diameters of 32 µm, because model transport is limited to this range.) The median fractional emission of clay-sized particles in the SMF experiment is 0.325, which is large compared to the AMF clay-sized fraction of 0.013 that is prescribed and based upon observations (cf. Eq. 9). The SMF median at each size is a function of the soil texture atlas. For

ACPD
15, 3493–3575, 2015

the AMF experiment, the median of the sum of the mass at silt sizes is also spatially uniform by prescription (cf. Eq. 10). Thus, individual silt bins exhibit smaller variability, compared to the SMF method, whose silt fraction varies with the local soil texture.

The annual-mean AMF surface concentration for different particle sizes is shown in Fig. 6a, b and c, along with its ratio with respect to the SMF values in Fig. 6d–f. The AMF global mean is 8.27 $\mu g\,m^{-3}$, consisting of 0.47 and 7.79 $\mu g\,m^{-3}$ at clay and silt sizes, respectively. The largest concentrations are located near the main source regions, including the Sahara and Sahel, the Arabian Peninsula, and Central Asia, where concentrations can exceed 500 $\mu g\,m^{-3}$. Large amounts of dust are also found in eastern Asia, Australia, and Patagonia, and smaller, yet regionally significant dust concentrations originate from source regions in the Great Plains of North America and Kalahari in southern Africa. The global surface concentration and load in the AMF experiment are less than half of their corresponding SMF values (Table 7, and Figs. 6d, and 7), a reduction that occurs despite identical total emission in both simulations (Fig. 8). (See Supplement Figs. S4 to S15 for gravitational settling, dry and wet deposition, and lifetime.) The smaller concentration and load in the AMF experiment results from its different assumption about the emitted size distribution compared to the SMF model. The SMF size distribution is determined by the local soil texture and its specified fractions of clay and silt-sized particles. In contrast, emission of the clay soil fraction is inhibited in the AMF model, an empirical constraint motivated by emission measurements. This results in a greater AMF silt fraction, compared to the SMF model. The larger particles are removed more quickly by gravitational setting, resulting in a smaller load and surface concentration in the AMF experiment. The reduction of AMF surface concentration compared to the SMF value is smallest over source regions, whereas the largest decreases are observed in remote regions of the tropics where the larger AMF particles have been removed by gravitational settling (Fig. 6d). The ratio of AMF global surface concentration at clay diameters compared to the SMF value is 0.05 (Fig. 6e), comparable to the ratio of clay emission (Fig. 8). This reflects the similar lifetime of clay particles in both experiments, reflecting wet removal as the common process that dom-

ACPD
15, 3493–3575, 2015

inates particle removal. At silt sizes, the global AMF concentration is 61 % larger than the SMF value (Fig. 6f), reflecting larger emission at this size in the former experiment. Note that the largest absolute contrasts between the two experiments are found near source regions, where total concentrations are several orders of magnitude higher than in remote regions.

4.2 Emitted mineral mass fractions

Contrasts between the experiments are apparent in the emitted fractions of the individual minerals, shown in Fig. 9. Within each size bin, distributions are calculated as in Fig. 5. The mass fractions are normalized so that *within each size bin*, their sum over all minerals is unity. This normalization is chosen to show the minerals making the largest median contribution to each size bin. To complement the bin fractions, the magnitude of global annual emission for each mineral is shown in Fig. 8.

The SMF emits clay-sized dust aerosols that are comprised mostly of phyllosilicates with median values of 0.40 for illite, 0.22 for smectite and 0.19 for kaolinite (Fig. 9, left). SMF phyllosilicates are absent among silt-sized aerosols, which are comprised mainly of quartz and feldspar, whose median values are 0.7 and 0.21, respectively. In the AMF, the mass fractions of clay-sized phyllosilicates are reduced in comparison to the SMF, offset by increases of feldspar and gypsum (Fig. 9, right). However, the AMF reintroduces phyllosilicates at silt sizes in proportion to γ, which is set equal to 2 in our reference AMF simulation. The effect of this reintroduction is to reduce the quartz and feldspar fractions in the silt size range. Calcite fractions at silt sizes are slightly increased compared to the SMF, particularly in the smallest silt-size model bins, due to the prescribed reaggregation of clay-sized soil particles. The use of observations to distribute the mass of each mineral across the silt size bins has significant effects (cf. Eq. (17) and Fig. 4). For example, the quartz fraction is distributed towards the larger silt-size bins, whose short lifetimes prevent significant dispersion downwind of the source region. In contrast, feldspar is enhanced toward the smaller silt size bins, whose shorter lifetime favors longer transport.

ACPD
15, 3493–3575, 2015

Figure 10 displays the emitted mineral fractions for the AMF experiment but without reaggregation of clay particles ($\gamma = 0$). The distribution of total dust mass in this simulation resembles that of our reference AMF (Fig. 6), because it necessarily satisfies Eq. (9). However, the effect of $\gamma = 0$ is to preclude the reaggregation of clay soil particles that would otherwise be emitted at silt sizes. The median fractions of quartz and feldspar in the silt size bins are higher than in the AMF experiment due to the absence of reaggregated phyllosilicates. This experiment will be used to identify the physical origin of contrasting behavior between the AMF and SMF methods in the companion article (Perlwitz et al., 2015).

4.3 Regional variations of the mineral fractions

4.3.1 Emission

The regional variations of emitted mineral fractions are displayed for illite and kaolinite (Fig. 11), quartz and carbonates (Fig. 12), and feldspar, gypsum, and iron oxides (Fig. 13). The left column shows the AMF emitted fraction, while the right column shows its ratio with respect to the SMF value. These global maps are shown at model resolution ($2^\circ \times 2.5^\circ$ latitude by longitude) and include only regions where dust emission occurs in our model. (Maps covering all soils where the MMT is applicable are provided in Figs. S1–S3 of the Supplement. Note that the extreme values depicted in the box plots in Fig. 9 are smoothed out at the model resolution due to spatial averaging.)

The AMF global fraction of emitted illite is 33 % in the clay size range (Fig. 11a) and 19 % over all sizes (Fig. 11b). The largest fractions are found in Northern Africa (specifically in Erg El Djouf between Mali and Mauritania, the Libyan Desert and the Qattarah Depression in Egypt), the Middle East (southern Saudi Arabia and Mesopotamia), Turkmenistan, the Tarim Basin and the Inner Mongolia deserts in east Asia, southern Australia, and the southern African coastal region. The AMF kaolinite global fraction is 25 % in the clay size range and 15 % for all sizes (Fig. 11c and d). In general, kaolinite

ACPD
15, 3493–3575, 2015

is largest where the illite fraction is lowest, specifically in the Sahel region, northwestern India, the Kalahari Desert in southern Africa and western Australia.

Illite, kaolinite, and smectite (the latter not shown) are absent at silt sizes in the SMF. The AMF extends these phyllosilicates into the silt size range (the size at which the prescribed fraction of emission is largest according to Fig. 5). This reaggregation is in proportion to their fraction as clay-sized particles in the wet-sieved soil, and results in an average increase when summed over all sizes of 27 % compared to the SMF (Fig. 11f and h). The global phyllosilicate fraction is decreased at clay sizes compared to the SMF by roughly 10 % (Fig. 11e and g) due to the inclusion of feldspar and gypsum.

The AMF global fraction of emitted quartz is roughly 7 % in the clay size range (Fig. 12a) and 34 % at silt sizes (Fig. 12b), with the largest values in sandy regions of southern Africa (Kalahari desert), northern Africa (Erg El Djouf between Mali and Mauritania, the Libyan Desert, northern Algeria and the Grand Erg of Bilma in Niger), northwestern India, southern Saudi Arabia, Turkmenistan and the Tarim Basin. Compared to the SMF, AMF quartz fractions are similar for clay sizes (Fig. 12e) and are lower by half in the silt size range (Fig. 12f).

The AMF global fraction of emitted carbonate is 5 and 6 % at clay and silt sizes, respectively (Fig. 12c and d), with the largest values in the North African coastal source regions (Algeria, Lybia and Egypt), Mesopotamia, the southern coast of the Saudi Arabia, the Iran–Afghanistan region, the Ganzu province in China, and the southern coasts of Africa and Australia. Carbonate fractions are low (less than 1 %) in the Sahel and the Kalahari Desert in southern Africa. At the native resolution of the soil texture and type databases, the clay-sized quartz and carbonate fractions are prescribed to be identical between the AMF and SMF experiments. Small differences at the model resolution arise from interpolation that is weighted by the different clay-sized fractions (Fig. 12e and g).

The AMF global fraction of emitted feldspar is roughly 13 % at both silt and all sizes (Fig. 13a and b), with the largest values in northern Africa (southern Algeria, northern Mauritania and northern Niger) and south of the Tarim Basin in East Asia. Compared

ACPD
15, 3493–3575, 2015

to the SMF experiment, the AMF global silt fraction of feldspar is 45 % lower (Fig. 13e), although at all sizes the fraction is only 6 % smaller (Fig. 13f).

Emission of gypsum and iron oxides is comparatively small, with local fractions never exceeding a few percent. The global emitted fraction of iron oxides is nearly identical in the AMF and SMF experiments (Fig. 13h). This agreement is fortuitous, resulting from the competing effects of reaggregation in the AMF experiment offset by the larger emitted clay fraction in the SMF experiment (Fig. 8). Emission of iron oxides is largest within the Sahel (Fig. 13d), where dust collected downwind is distinguished by its reddish color (Carlson and Prospero, 1972). Smaller enrichment of iron oxides is seen within the Kalahari Desert of southern Africa, as well as eastern Australia along with the Thar Desert and maritime foothills of the Western Ghats within the Indian subcontinent.

4.3.2 Surface concentration

Figures 14 and 15 display the global distribution of the annual-average mineral fractions in surface concentration for the AMF, along with their ratio with respect to the SMF fractions.

Attribution of the mineral fractions to contrasts between the AMF and SMF methods is challenging because the fractional surface concentration depends upon the interaction of numerous processes including the size dependence of emission and removal, along with the proximity of sources enriched or depleted in different minerals. Nonetheless, the figures illustrate the effect of some physical assumptions underlying the methods and contrasts between them. For example, the AMF kaolinite and iron oxide fractions are large downwind of the Sahel and southern Africa (Figs. 14b and 15c), where the source regions are enriched in these minerals (Figs. 11 and 13). Similarly, the fractional concentrations of quartz and feldspar are enriched along the Pacific coast of South America (Fig. 15a and b), reflecting their origin from local sources, including Patagonia, along with the shielding effect of the Andes that limits transport from Africa. Conversely, the tropical western Pacifc is depleted in quartz and gypsum

ACPD
15, 3493–3575, 2015

(Fig. 15a and d), because emission of these minerals is relatively small upwind over Australia. In general, the concentration of illite is inversely related to that of kaolinite (Fig. 14a and b), reflecting the contrasting weathering processes that create each mineral in the source soil.

Differences between the AMF and SMF methods are also illustrated. Far from source regions, clay-sized particles dominate the concentration. Thus, the difference of the clay-sized fractions of emission determines approximately whether the concentration of a particular mineral in remote regions is larger according to one method. (This relation is approximate, because some clay-sized minerals may be removed preferentially due to the proximity of their sources to regions of enhanced precipitation and wet removal.) For example, the clay-sized fraction of phyllosilicates is smaller in the AMF experiment (Figs. 9), so their ratio with respect to the SMF decreases downwind (Fig. 14e–g). This contrast is enhanced by the greater SMF fractional emission of clay particles (Fig. 5). Conversely, the ratios of gypsum and feldspar increase downwind (Fig. 15f and h), because clay-sized emission of these minerals occurs only in the AMF experiment. The ratio of AMF quartz also increases downstream (Fig. 15e), although attribution is more elusive, because the emitted clay-sized fraction is nearly identical in both experiments. In general, the global-mean ratio of the AMF and SMF fractional concentration for each mineral reflects the ratio of the two experiments far from the source.

Immediately downwind from a source region enriched in phyllosilicates and iron oxides, the ratio of the AMF and SMF fractional concentrations decrease (Figs. 14e–g and 15g). This is because their emission is peaked toward larger sizes in the AMF experiment, so that the fractional concentration of a particular mineral falls off within a shorter distance of a source region where it is enriched.

4.4 Iron oxides: pure vs. accreted forms

The fraction of iron oxide in accreted form (based upon column mass) is shown in Fig. 16a. The accreted fraction is smallest downwind of the Sahel and other source regions enriched in iron oxides (Fig. 16a). These minima are a consequence of our

ACPD
15, 3493–3575, 2015

mixing assumption, Eq. (22), that increases the fraction of pure crystalline iron oxide where the soil is enriched in this mineral (Fig. 13g). The accreted fraction increases downwind as the pure crystalline form is removed preferentially by gravity due to its greater density.

Regions where the soil is enriched in iron oxides correspond to a maximum of accreted iron oxide mass relative to the total dust mass (Fig. 16b), even if a larger proportion of this mineral is in pure crystalline form according to Eq. (22) and Fig. 16a. The AMF global mass fraction of accreted iron oxide is 1.82 %, within the range of values typically assumed by models that relate dust radiative properties to (globally uniform) prescribed mineral composition (Sokolik and Toon, 1999; Balkanski et al., 2007). This fraction results from two assumptions in our model: first, that iron oxides are 5 % of the particle mass (Eq. 25), and second, that the assumed fraction of accreted iron oxide decreases in enriched soils, according to Eq. (22) and our choice of ϵ_0. There are few observations to constrain precise values of either of these parameters, although the primary contribution of iron oxide to measured aerosol radiative absorption offers an indirect constraint. The accreted fraction is presumably insensitive to a range of R. A larger prescribed value would distribute the accreted iron oxide over fewer particles, while a smaller value would result in accretions within more particles. The accreted fraction of iron oxides in our model is presumably more sensitive to the prescribed partitioning of crystalline and accreted forms according to Eq. (22) that is a heuristic attempt to represent the effect of soil weathering.

The fraction of quartz and phyllosilicates containing iron oxide accretions compared to the total dust mass is shown in Fig. 16c and d, respectively. This fraction is largest in regions enriched in iron oxides, but also where the fractions of the host minerals are large, according to Eq. (26). The total fractional mass of dust particles containing accretions is largest downwind of soils enriched in iron oxides (Fig. 16e). The global mass fraction is 34.60 %. We can calculate the effective mixing fraction of iron oxide to the total particle mass as $\frac{1.82}{34.60+1.82} = 0.04997$ that can be compared to our chosen value of $R = 0.05$. The discrepancy originates within regions of iron oxide-rich soils,

ACPD
15, 3493–3575, 2015

where the accreted fraction, given by Eq. (24), is so large that there is an insufficient supply of other minerals available for mixing (necessitating the minimum operator as an upper bound in Eq. 29). The small difference between the prescribed value of R and its effective value indicates that the exhaustion of other minerals available to host accretions occurs at only a few locations.

We carried out additional experiments to illustrate the effect of our model assumptions for iron oxides and its mixtures (Table 9, and Figs. S16 and S17 in the Supplement). The introduction of iron oxides at clay sizes following Nickovic et al. (2012) results in global iron oxide mass that is five times larger compared to the SMF-NoClayFe experiment that emits iron oxides only at silt sizes following Claquin et al. (1999). This contrast results from the large fraction of clay particles in the wet-sieved soil characterized by Claquin et al. (1999) and the correspondingly large clay emission.

The effect of accretions is shown by contrasting the AMF and AMF-NoFeAcc experiments. The iron oxide mass at clay sizes is nearly identical in the two experiments because removal of this particle size is dominated by wet deposition that is independent of particle density. However, at larger silt sizes, whose concentration is more vulnerable to removal by gravitational settling, the AMF experiment with accretions has a global iron oxide mass that is larger by 40 %.

4.5 Evaluation at Tinfou, Morroco

A detailed comparison of the model to observations is presented in a companion article (Perlwitz et al., 2015), where we use a global compilation of measurements from almost sixty studies. In the present study, we compare the mineral fractions of the AMF and the SMF surface concentration to measurements at Tinfou, Morroco (Figs. 17 and 18). While we have used these measurements to distribute the emitted mass of each mineral within the silt size range, the observed fractions of surface concentration are not prescribed within our model. The model concentration is affected by local emission, but also by advection from other sources, and processes such as turbulent mixing and

ACPD
15, 3493–3575, 2015

deposition. Therefore, the observed fractions of surface concentration are a collective test of these model processes, along with the accuracy of the MMT.

Figure 17 shows the fractional contribution of each mineral to surface concentration. (Smectite is omitted, because it is not measured.) These fractions sum to unity at each size bin, so that comparison to measurements shows each model's ability to reproduce the fractional contribution of minerals within separate size classes. In the SMF experiment, phyllosilicates are missing from all silt-size bins, as are feldspar and gypsum from the clay-size bins. The AMF method improves the representation of these minerals through reaggregation that restores phyllosilicates to the silt range and brittle fragmentation that creates feldspar and gypsum at clay sizes. Another distinctive feature of the SMF experiment is the strong overestimation of the quartz fraction at silt sizes. This is largely corrected by the AMF method that increases the phyllosilicate fraction of emitted silt at the expense of quartz. This is shown by the AMF fractions calculated with $\gamma = 3.5$, where enhanced reaggregation at silt sizes leads to an additional increase of phyllosilicates and a reduction of quartz. The AMF method overestimates the kaolinite fraction at all sizes. The common error of the AMF and SMF experiments at clay sizes suggests that the kaolinite fraction may be overestimated by the MMT, although other processes like transport can contribute to the error. The AMF kaolinite fraction at silt sizes is sensitive to its prescribed MMT fraction at clay sizes due to reaggregation, as shown by the increased error for $\gamma = 3.5$.

Feldspar is the exceptional mineral where the SMF fraction is more realistic at all silt sizes. The AMF experiment underestimates the measured feldspar fraction, although it predicts a non-zero fraction at clay sizes in contrast to the SMF experiment. In the companion article, we show that the AMF feldspar fraction is generally in better agreement at other locations. Both methods underestimate the iron oxide fraction, and the discrepancy of the SMF value increases with particle diameter due to the absence of internal mixtures. The relatively large density of the pure crystalline form enhances gravitational removal, reducing the particle lifetime as diameter increases. In contrast, the internal

ACPD
15, 3493–3575, 2015

mixtures present in the AMF experiment are removed more slowly, reproducing the measured weak dependence of the iron oxide fraction upon particle size.

Figure 18 shows mineral fractions, but without separate normalization within each size bin. That is, the fractions sum to unity over all minerals and all sizes. Fidelity in comparison to the measurements at Tinfou depends additionally upon the ability of each experiment to reproduce the measured size distribution. The SMF experiment strongly overestimates the clay size fractions due to its relatively large emission at this size (Fig. 8). In contrast, the AMF fractions are closer to the measured values due to their smaller emitted clay fraction. The most consistent error in the AMF experiment is an underestimate of each mineral fraction within the largest size category. This behavior is partly the result of using measurements of surface concentration to distribute the emitted mass within the silt size bins according to Eq. (17). The emitted size distribution is modified by deposition, which preferentially removes the largest particles by gravitational settling. We try to limit the influence of deposition by using the aerosol size distribution measured during times of high surface concentration when emission is presumably recent. However, the use of concentration will inevitably lead to a negative bias that future model versions will have to address.

The measurements at Tinfou are exceptional among the literature for their range of characterization, but Kandler et al. (2009) note that feldspar and the phyllosilicates are difficult to distinguish, resulting in these minerals being assigned the same fractional distribution of mass with respect to size (Fig. 4). Measurements of elemental composition (their Fig. 14) suggest that the mass of feldspar may increase relative to phyllosilicates at larger silt sizes. This would not narrow the discrepancy of the AMF fractions at these sizes (since the refined measurements would also modify the prescribed size distribution of silt in all our experiments according to Eq. 17). However, the uncertain distinction between the measured size distributions of feldspar and phyllosilicates has implications for the transport of both minerals. An increase of feldspar at larger sizes (with a corresponding decrease at smaller sizes due to the normalization of the size distribution) would confine this mineral more closely to its source region. Conversely,

ACPD
15, 3493–3575, 2015

a decrease of phyllosilicates at larger sizes would correspond to greater abundance and dispersal at smaller sizes with corresponding impacts upon global climate, for example, through ice nucleation (Hoose et al., 2008). We will revisit the effects of this uncertainty of the mineral size distributions in the companion article (Perlwitz et al., 2015).

5 Conclusions

Aerosol mineral composition depends upon the composition of the parent soil and its size fractionation during mobilization. Soil mineral fractions have been estimated using atlases of arid soil type and soil texture by Claquin et al. (1999). However, these authors identify the additional challenge of accounting for the effect of wet sieving in both atlases that alters the soil particle size distribution by breaking aggregates.

We have proposed an empirical method to reconstruct the mineral fractions in the undisturbed soil that is subject to wind erosion. We assume that some of the emitted silt-size particles originated in the clay-sized fraction of the wet-sieved soil (Eq. 11), whose mineral fractions are estimated by Claquin et al. (1999). We also account for subsequent distintegration during emission by imposing fractions of clay and silt-sized particles based upon size-resolved measurements of emission (cf. Kok, 2011).

In addition, we create an additional class of iron oxide aerosol that is a small impurity embedded within other minerals, allowing it to travel farther than in its pure crystalline state. We assume that these impurities are least frequent in soils rich in iron oxides (as a result of the assumed effect of weathering to create pure iron oxide crystals). Nonetheless, the abundance of iron oxide in these soils means that the absolute value of iron oxides in accretions is large. We assume that iron oxides contribute 5 % to the combined particle mass. The remainder is transported in pure crytalline form and falls out quickly due to its higher density, so total global iron oxide fraction is just under 2 %. Our treatment of iron oxides is constrained by relatively few observations and subject to more precise future treatments. Nonetheless, modeling of aerosol iron is important

ACPD
15, 3493–3575, 2015

for its influence upon several climate processes, including aerosol radiative forcing and marine photosynthesis that modulates atmospheric carbon dioxide.

These extensions define our AMF experiment. In contrast, the SMF experiment serves as a control whose emitted size distribution is taken directly from that of the wet-sieved soil and excludes iron accretions. For both experiments, we calculate the regional distribution of minerals using the NASA GISS ModelE2, whose dust size categories range in diameter from 0.1 to 32 µm.

Emission of clay-sized particles is much smaller in the AMF experiment, due to the empricial constraint upon the emitted size distribution. This has implications for long-range transport. Both the SMF and AMF have identical emission (by construction), but the column load and surface concentration are much lower in the latter experiment, because the particles are larger. Nonetheless, the emission of clay minerals (i.e. phyllosilicates) is only slightly smaller in the AMF experiment. This is a consequence of reaggregation of the wet-sieved soil that results in a substantial fraction of phyllosilicate particles at silt sizes.

In companion articles (Perlwitz et al., 2015; Pérez García-Pando et al., 2015), we compare the AMF and SMF experiments to measurements. In the present article, our comparison is limited to the mineral fractions of surface concentration measured at Tinfou, Morocco (Kandler et al., 2009). These show a majority of the phyllosilicate (or "clay" mineral) mass at silt sizes, consistent with our AMF method. In spite of the substantially greater silt-sized emission of this method compared to the SMF, both experiments predict comparable fractions of quartz. This agreement is the result of the reaggregation of clay minerals that reduces the quartz fraction at silt sizes in the undispersed soil prior to emission. This reduction occurs because total silt emission of all minerals is fixed by our empirical constraint Eq. (10). The reduction also occurs because we account for the larger characteristic size of quartz in the parent soil compared to other minerals. The aerosol size distribution measured by Kandler et al. (2009) suggests that a disproportionate amount of quartz at silt sizes is beyond the size range that is dispersed far from the source. This shows the value of measurements that can distinguish potential

ACPD
15, 3493–3575, 2015

differences among the mineral size distributions. We have noted how the distinction between the size distributions of phyllosilicates and feldspar have implications for long-range transport and climate impacts like ice nucleation (Hoose et al., 2008; Atkinson et al., 2013).

In general, our empirical reconstruction of the undispersed soil allows us to shift clay-sized phyllosilicates in the wet-sieved soil toward silt sizes where they are observed and maintain realistic fractions of quartz, despite the observed size distribution of the emitted aerosol that is heavily biased toward silt sizes. We have made little effort to find the optimal amount of reaggregation. Instead, we are developing a more physically based model of reaggregation and brittle fragmentation that extends studies by Kok (2011) and Scanza et al. (2015), while addressing certain inconsistencies of our present semi-empirical approach. (For example, we presently reaggregate minerals in proportion to s_c, the local fraction of clay-sized particles given by the soil texture atlas, but assume a uniform fraction of clay-sized emission according to Eq. (9) that is independent of this texture.) More generally, we will take advantage of more recent estimates of soil mineral fraction (Journet et al., 2014) that use additional measurements to extend the method of Claquin et al. (1999). Singular soil environments like the Bodélé Depression and littoral margins of Lake Chad, where concentrations of diatomite and other constituents derived from biological processes are large, present an additional challenge that results from their significant contribution to global dust emission (Washington et al., 2009).

Appendix A

Here we use the assumptions in Sect. 2.2.2 to derive the mass fraction of the iron oxide mixture given by Eq. (29), along with the remaining mass fractions of iron oxides (Eq. 30) and mineral n (Eq. 31) in their pure unmixed state.

We have assumed that accreted iron oxides contribute fraction R to the total mass of the particle mixture via Eq. (25). For small enough prescribed fractions of accretion

ACPD
15, 3493–3575, 2015

($R \ll 1$), there will be an insufficient amount of the other mineral to combine with the amount of iron oxides specified by Eq. (24). This follows from Eq. (18):

$$d_{n,k}^{\text{mix}} \leq d_{n,k}, \tag{A1}$$

so that from Eq. (25):

$$d_{\text{Fe}|n,k}^{\text{mix}} \leq \frac{R}{1-R} d_{n,k}. \tag{A2}$$

In general,

$$d_{\text{Fe}|n,k}^{\text{mix}} = \min\left[(1-d_{\text{Fe},k})d_{\text{Fe},k}\frac{d_{n,k}}{\overline{d}_k}, \frac{R}{1-R}d_{n,k}\right]. \tag{A3}$$

Then, the emitted mass fraction of the prognostic variable comprised of mineral n and iron oxides is:

$$d_{n,k}^{\text{mix}} + d_{\text{Fe}|n,k}^{\text{mix}} = \min\left[\frac{(1-d_{\text{Fe},k})d_{\text{Fe},k}}{R}\frac{d_{n,k}}{\overline{d}_k}, \frac{d_{n,k}}{1-R}\right] \tag{29}$$

Again, $d_{\text{Fe},k}$ and $d_{n,k}$ that are inputs to Eqs. (A3) and (29) are given by Eqs. (12)–(15) and (17).

The pure or unmixed mass fraction of each mineral can be derived from Eq. (A3). Using Eqs. (18) and (25) it can be shown that:

$$d_{n,k}^{\text{pure}} = d_{n,k} - \left(\frac{1-R}{R}\right) d_{\text{Fe}|n,k}^{\text{mix}}, \tag{31}$$

and:

$$\begin{aligned} d_{\text{Fe},k}^{\text{pure}} &= d_{\text{Fe},k} - \sum_{n \neq \text{iron oxide}} d_{\text{Fe}|n,k}^{\text{mix}} \\ &= d_{\text{Fe},k} - \min\left[\left(1-d_{\text{Fe},k}\right)d_{\text{Fe},k}, \frac{R}{1-R}\sum_{n \neq \text{iron oxide}} d_{n,k}\right] \end{aligned} \tag{A4}$$

ACPD
15, 3493–3575, 2015

so that:

$$d_{\mathrm{Fe},k}^{\mathrm{pure}} = d_{\mathrm{Fe},k} - \min\left[\left(1 - d_{\mathrm{Fe},k}\right) d_{\mathrm{Fe},k}, \frac{R}{1-R}\overline{d}_k\right]. \tag{30}$$

For the case where the mass fraction of the emitted iron oxides is small enough, so that:

$$\left(1 - d_{\mathrm{Fe},k}\right) d_{\mathrm{Fe},k} \leq \frac{R}{1-R}\overline{d}_k, \tag{A5}$$

all the iron oxides available for mixing can be combined with the other minerals, and Eq. (30) reduces to Eq. (23).

The Supplement related to this article is available online at doi:10.5194/acpd-15-3493-2015-supplement.

Acknowledgements. We thank Paul Ginoux, Konrad Kandler, Natalie Mahowald, Sergio Rodríguez and Rachel Scanza for helpful conversations. This research was supported by the National Science Foundation (ATM-01-24258), the Department of Energy (DE-SC0006713), the NASA Modeling, Analysis and Prediction Program and the Ministry of Economy and Competitiveness of Spain through the POLLINDUST project (CGL2011-26259). Computational resources were provided by the NASA High-End Computing (HEC) Program through the NASA Center for Climate Simulation (NCCS) at Goddard Space Flight Center. The data file with the mineral fractions at emission for the AMF method at a resolution of $5' \times 5'$ latitude by longitude is available online at the website of the NASA Goddard Institute for Space Studies: http://data.giss.nasa.gov/mineralfrac/.

ACPD
15, 3493–3575, 2015

References

Alastuey, A., Querol, X., Castillo, S., Escudero, M., Avila, A., Cuevas, E., Torres, C., Romero, P.-M., Exposito, F., García, O., Diaz, J. P., Van Dingenen, R., and Putaud, J. P.: Characterisation of TSP and $PM_{2.5}$ at Izaña and Sta. Cruz de Tenerife (Canary Islands, Spain) during a Saharan Dust Episode (July 2002), Atmos. Environ., 39, 4715–4728, doi:10.1016/j.atmosenv.2005.04.018, 2005. 3500

Albani, S., Mahowald, N. M., Perry, A. T., Scanza, R. A., Zender, C. S., Heavens, N. G., Maggi, V., Kok, J. F., and Otto-Bliesner, B. L.: Improved dust representation in the Community Atmosphere Model, J. Adv. Model. Earth Syst., 6, 541–570, doi:10.1002/2013MS000279, 2014. 3505

Alfaro, S. C. and Gomes, L.: Modeling mineral aerosol production by wind erosion: emission intensities and aerosol size distributions in source areas., J. Geophys. Res., 106, 18075–18084, doi:10.1029/2000JD900339, 2001. 3496, 3503

Atkinson, J. D., Murray, B. J., Woodhouse, M. T., Whale, T. F., Baustian, K. J., Carslaw, K. S., Dobbie, S., O'Sullivan, D., and Malkin, T. L.: The importance of feldspar for ice nucleation by mineral dust in mixed-phase clouds, Nature, 498, 355–358, doi:10.1038/nature12278, 2013. 3495, 3496, 3499, 3502, 3534

Balkanski, Y., Schulz, M., Claquin, T., and Guibert, S.: Reevaluation of Mineral aerosol radiative forcings suggests a better agreement with satellite and AERONET data, Atmos. Chem. Phys., 7, 81–95, doi:10.5194/acp-7-81-2007, 2007. 3502, 3515, 3528

Bian, H. and Zender, C. S.: Mineral dust and global tropospheric chemistry: relative roles of photolysis and heterogeneous uptake, J. Geophys. Res., 108, 4672, doi:10.1029/2002JD003143, 2003. 3495

Bian, H., Prather, M. J., and Takemura, T.: Tropospheric aerosol impacts on trace gas budgets through photolysis, J. Geophys. Res., 108, 4242, doi:10.1029/2002JD002743, 2003. 3495

Cakmur, R. V., Miller, R. L., and Torres, O.: Incorporating the effect of small-scale circulations upon dust emission in an atmospheric general circulation model, J. Geophys. Res., 109, D07201, doi:10.1029/2003JD004067, 2004. 3517

Caquineau, S., Gaudichet, A., Gomes, L., Magonthier, M., and Chatenet, B.: Saharan dust: Clay ratio as a relevant tracer to assess the origin of soil – derived aerosols, Geophys. Res. Lett., 25, 983–986, doi:10.1029/98GL00569, 1998. 3500

ACPD
15, 3493–3575, 2015

Carlson, T. N. and Prospero, J. M.: The Large-Scale Movement of Saharan Air Outbreaks over the Northern Equatorial Atlantic, J. Appl. Meteorol., 11, 283–297, doi:10.1175/1520-0450(1972)011<0283:TLSMOS>2.0.CO;2, 1972. 3526

Chatenet, B., Marticorena, B., Gomes, L., and Bergametti, G.: Assessing the microped size distributions of desert soils erodible by wind, Sedimentology, 43, 901–911, doi:10.1111/j.1365-3091.1996.tb01509.x, 1996. 3499

Chen, H., Navea, J. G., Young, M. A., and Grassian, V. H.: Heterogeneous photochemistry of trace atmospheric gases with components of mineral dust aerosol, J. Phys. Chem. A, 115, 490–499, doi:10.1021/jp110164j, 2011. 3495

Chesworth, W. (Ed.): Encyclopedia of Soil Sciences, Springer, Dordrecht, Berlin, Heidelberg, New York, doi:10.1007/978-1-4020-3995-9, 2008. 3515

Choate, L. M., Ranville, J. F., Bunge, A. L., and Macalady, D. L.: Dermally adhered soil: 2. Reconstruction of dry-sieve particle-size distributions from wet-sieve data, Int. Environ. Assess. Manage., 2, 385–390, doi:10.1002/ieam.5630020410, 2006. 3496, 3498

Claquin, T., Schulz, M., and Balkanski, Y. J.: Modeling the mineralogy of atmospheric dust sources, J. Geophys. Res., 104, 22243–22256, doi:10.1029/1999JD900416, 1999. 3496, 3498, 3499, 3501, 3503, 3505, 3507, 3508, 3520, 3529, 3532, 3534, 3549, 3550

d'Almeida, G. A. and Schütz, L.: Number, mass and volume distributions of mineral aerosol and soils of the Sahara, J. Clim. Appl. Meteorol., 22, 233–243, doi:10.1175/1520-0450(1983)022<0233:NMAVDO>2.0.CO;2, 1983. 3504

Deboudt, K., Gloter, A., Mussi, A., and Flament, P.: Red-ox speciation and mixing state of iron in individual African dust particles, J. Geophys. Res., 117, D12307, doi:10.1029/2011JD017298, 2012. 3496

DeMott, P. J., Sassen, K., Poellot, M. R., Baumgardner, D., Rogers, D. C., Brooks, S. D., Prenni, A. J., and Kreidenweis, S. M.: African dust aerosols as atmospheric ice nuclei, Geophys. Res. Lett., 30, 1732, doi:10.1029/2003GL017410, 2003. 3495

Dentener, F. J., Carmichael, G. R., Zhang, Y., Lelieveld, J., and Crutzen, P. J.: Role of mineral aerosol as a reactive surface in the global troposphere, J. Geophys. Res., 101, 22869–22889, doi:10.1029/96JD01818, 1996. 3495

FAO: Digital Soil Map of the World and Derived Soil Properties, Food and Agriculture Organization, Rome, Italy, 1995. 3498

FAO: Digital Soil Map of the World, Food and Agriculture Organization, Rome, Italy, 2007. 3498, 3507, 3549

ACPD
15, 3493–3575, 2015

FAO/IIASA/ISRIC/ISSCAS/JRC: Harmonized World Soil Database (version 1.2), FAO, Rome, Italy and IIASA, Laxenburg, Austria, available at: http://webarchive.iiasa.ac.at/Research/LUC/External-World-soil-database/HTML/HWSD_Data.html?sb=4, last access date: 24 January 2013, 2012. 3507, 3549

Feingold, G., Cotton, W. R., Kreidenweis, S. M., and Davis, J. T.: The impact of giant cloud condensation nuclei on drizzle formation in stratocumulus: implications for cloud radiative properties, J. Atmos. Sci., 56, 4100–4117, doi:10.1175/1520-0469(1999)056<4100:TIOGCC>2.0.CO;2, 1999. 3495

Frinak, E. K., Mashburn, C. D., Tolbert, M. A., and Toon, O. B.: Infrared characterization of water uptake by low-temperature Na-montmorillonite: implications for Earth and Mars, J. Geophys. Res., 110, D09308, doi:10.1029/2004JD005647, 2005. 3495

Gillette, D. A.: On the production of soil wind erosion aerosols having the potential for long range transport, J. Rech. Atmos., 8, 735–744, 1974. 3503, 3504

Gillette, D. A., Blifford Jr., I. H., and Fenster, C. R.: Measurements of aerosol size distributions and vertical fluxes of aerosols on land subject to wind erosion, J. Appl. Meteorol., 11, 977–987, doi:10.1175/1520-0450(1972)011<0977:MOASDA>2.0.CO;2, 1972. 3503, 3504

Gillette, D. A., Blifford J. R., I. H., and Fryrear, D. W.: The Influence of Wind Velocity on the size distributions of aerosols generated by the wind erosion of soils, J. Geophys. Res., 79, 4068–4075, doi:10.1029/JC079i027p04068, 1974. 3496, 3503, 3504

Ginoux, P., Chin, M., Tegen, I., Prospero, J. M., Holben, B., Dubovik, O., and Lin, S.-J.: Sources and distributions of dust aerosols simulated with the GOCART model, J. Geophys. Res., 106, 20255–20273, doi:10.1029/2000JD000053, 2001. 3518

Glaccum, R. A. and Prospero, J. M.: Saharan aerosols over the tropical North Atlantic – Mineralogy, Mar. Geol., 37, 295–321, doi:10.1016/0025-3227(80)90107-3, 1980. 3501

Goldstein, H., Reynolds, R., Reheis, M., Yount, J., Lamothe, P., Roberts, H., and McGeehin, J.: Particle Size, CaCO3, Chemical, Magnetic, and Age Data from Surficial Deposits in and around Canyonlands National Park, Utah, Open-file report 2005-1186, U. S. Geological Survey, Reston, Virginia, available at: http://pubs.usgs.gov/of/2005/1186, last access date: 8 September 2014, 2005. 3504

Goodman, A. L., Underwood, G. M., and Grassian, V. H.: A laboratory study of the heterogeneous reaction of nitric acid on calcium carbonateparticles, J. Geophys. Res., 105, 29053–29064, doi:10.1029/2000JD900396, 2000. 3495

ACPD
15, 3493–3575, 2015

Grini, A., Zender, C. S., and Colarco, P. R.: Saltation Sandblasting behavior during mineral dust aerosol production, Geophys. Res. Lett., 29, 1868, doi:10.1029/2002GL015248, 2002. 3496, 3503

Hatch, C. D., Gierlus, K. M., Schuttlefield, J. D., and Grassian, V. H.: Water adsorption and cloud condensation nuclei activity of calcite and calcite coated with model humic and fulvic acids, Atmos. Environ., 42, 5672–5684, doi:10.1016/j.atmosenv.2008.03.005, 2008. 3495

Hatch, C. D., Greenaway, A. L., Christie, M. J., and Baltrusaitis, J.: Water adsorption constrained Frenkel–Halsey-Hill adsorption activation theory: Montmorillonite and illite, Atmos. Environ., 87, 26–33, doi:10.1016/j.atmosenv.2013.12.040, 2014. 3495

Hoose, C. and Möhler, O.: Heterogeneous ice nucleation on atmospheric aerosols: a review of results from laboratory experiments, Atmos. Chem. Phys., 12, 9817–9854, doi:10.5194/acp-12-9817-2012, 2012. 3495

Hoose, C., Lohmann, U., Erdin, R., and Tegen, I.: The global influence of dust mineralogical composition on heterogeneous ice nucleation in mixed-phase clouds, Environ. Res. Lett., 3, 025003, doi:10.1088/1748-9326/3/2/025003, 2008. 3496, 3499, 3502, 3532, 3534

Huneeus, N., Schulz, M., Balkanski, Y., Griesfeller, J., Prospero, J., Kinne, S., Bauer, S., Boucher, O., Chin, M., Dentener, F., Diehl, T., Easter, R., Fillmore, D., Ghan, S., Ginoux, P., Grini, A., Horowitz, L., Koch, D., Krol, M. C., Landing, W., Liu, X., Mahowald, N., Miller, R., Morcrette, J.-J., Myhre, G., Penner, J., Perlwitz, J., Stier, P., Takemura, T., and Zender, C. S.: Global dust model intercomparison in AeroCom phase I, Atmos. Chem. Phys., 11, 7781–7816, doi:10.5194/acp-11-7781-2011, 2011. 3518

Ito, A.: Contrasting the effect of iron mobilization on soluble iron deposition to the ocean in the Northern and Southern Hemispheres, J. Meteorol. Soc. Jpn. A, 90, 167–188, doi:10.2151/jmsj.2012-A09, 2012. 3495

Iversen, J. D. and White, B. R.: Saltation threshold on Earth, Mars and Venus, Sedimentology, 29, 111–119, doi:10.1111/j.1365-3091.1982.tb01713.x, 1982. 3500

Iversen, J. D., Greeley, R., and Pollack, J. B.: Windblown dust on Earth, Mars and Venus, J. Atmos. Sci., 33, 2425–2429, doi:10.1175/1520-0469(1976)033<2425:WDOEMA>2.0.CO;2, 1976. 3500

Jeong, G. Y.: Bulk and single-particle mineralogy of Asian dust and a comparison with its source soils, J. Geophys. Res., 113, D02208, doi:10.1029/2007JD008606, 2008. 3501

ACPD
15, 3493–3575, 2015

Jeong, G. Y. and Nousiainen, T.: TEM analysis of the internal structures and mineralogy of Asian dust particles and the implications for optical modeling, Atmos. Chem. Phys., 14, 7233–7254, doi:10.5194/acp-14-7233-2014, 2014. 3500, 3501

Jickells, T. D., An, Z. S., Andersen, K. K., Baker, A. R., Bergametti, G., Brooks, N., Cao, J. J., Boyd, P. W., Duce, R. A., Hunter, K. A., Kawahata, H., Kubilay, N., laRoche, J., Liss, P. S., Mahowald, P. S. N., Prospero, J. M., Ridgwell, A. J., Tegen, I., and Torres, R.: Global iron connections between desert dust, ocean biogeochemistry, and climate, Science, 308, 67–71, doi:10.1126/science.1105959, 2005. 3495

Johnson, D. B.: The role of giant and ultragiant aerosol particles in warm rain initiation, J. Atmos. Sci., 39, 448–460, doi:10.1175/1520-0469(1982)039<0448:TROGAU>2.0.CO;2, 1982. 3495

Journet, E., Desboeufs, K. V., Caquineau, S., and Colin, J.-L.: Mineralogy as a critical factor of dust iron solubility, Geophys. Res. Lett., 35, L07805, doi:10.1029/2007GL031589, 2008. 3500

Journet, E., Balkanski, Y., and Harrison, S. P.: A new data set of soil mineralogy for dust-cycle modeling, Atmos. Chem. Phys., 14, 3801–3816, doi:10.5194/acp-14-3801-2014, 2014. 3496, 3498, 3499, 3534

Kandler, K., Benker, N., Bundke, U., Cuevas, E., Ebert, M., Knippertz, P., Rodríguez, S., Schütz, L., and Weinbruch, S.: Chemical composition and complex refractive index of Saharan Mineral Dust at Izan, Tenerife (Spain) derived by electron microscopy, Atmos. Environ., 41, 8058–8074, doi:10.1016/j.atmosenv.2007.06.047, 2007. 3502, 3513

Kandler, K., Schütz, L., Deutscher, C., Ebert, M., Hofmann, H., Jäckel, S., Jaenicke, R., Knippertz, P., Lieke, K., Massling, A., Petzold, A., Schladitz, A., Weinzierl, B., Wiedensohler, A., Zorn, S., and Weinbruch, S.: Size distribution, mass concentration, chemical and mineralogical composition and derived optical parameters of the boundary layer aerosol at Tinfou, Morocco, during SAMUM 2006, Tellus B, 61, 32–50, doi:10.1111/j.1600-0889.2008.00385.x, 2009. 3499, 3505, 3506, 3510, 3511, 3513, 3517, 3520, 3531, 3533, 3549, 3550, 3558, 3560, 3561, 3574

Kandler, K., Schütz, L., Jäckel, S., Lieke, K., Emmel, C., Müller-Ebert, D., Ebert, M., Scheuvens, D., Schladitz, A., Šegvić, B., Wiedensohler, A., and Weinbruch, S.: Ground-based off-line aerosol measurements at Praia, Cape Verde, during the Saharan Mineral Dust Experiment: microphysical properties and mineralogy, Tellus B, 63, 459–474, doi:10.1111/j.1600-0889.2011.00550.x, 2011. 3501

ACPD
15, 3493–3575, 2015

Kelly, J. T., Chuang, C. C., and Wexler, A. S.: Influence of dust composition on cloud droplet formation, Atmos. Environ., 41, 2904–2916, doi:10.1016/j.atmosenv.2006.12.008, 2007. 3495
Koch, D., Jacob, D., Tegen, I., Rind, D., and Chin, M.: Tropospheric sulfur simulation and sulfate direct radiative forcing in the Goddard Institute for Space Studies general circulation model, J. Geophys. Res., 104, 23799–23822, doi:10.1029/1999JD900248, 1999. 3519
Kok, J. F.: A scaling theory for the size distribution of emitted dust aerosols suggests climate models underestimate the size of the global dust cycle, P. Natl. Acad. Sci. USA, 108, 1016–1021, doi:10.1073/pnas.1014798108, 2011. 3496, 3497, 3500, 3503, 3504, 3505, 3506, 3509, 3511, 3532, 3534, 3559, 3560
Koven, C. D. and Fung, I.: Inferring dust composition from wavelength-dependent absorption in Aerosol Robotic Network (AERONET) data, J. Geophys. Res., 111, D14205, doi:10.1029/2005JD006678, 2006. 3515
Krueger, B. J., Grassian, V. H., Cowin, J. P., and Laskin, A.: Heterogeneous chemistry of individual mineral dust particles from different dust source regions: the importance of particle mineralogy, Atmos. Environ., 38, 6253–6261, doi:10.1016/j.atmosenv.2004.07.010, 2004. 3495
Lafon, S., Sokolik, I. N., Rajot, J. L., Caquineau, S., and Gaudichet, A.: Characterization of iron oxides in mineral dust aerosols: implications for light absorption, J. Geophys. Res., 111, D21207, doi:10.1029/2005JD007016, 2006. 3513
Laurent, B., Marticorena, B., Bergametti, G., Léon, J. F., and Mahowald, N. M.: Modeling mineral dust emissions from the Sahara desert using new surface properties and soil database, J. Geophys. Res.-Atmos., 113, D14218, doi:10.1029/2007JD009484, 2008. 3496, 3498, 3499
Leinen, M., Prospero, J. M., Arnold, E., and Blank, M.: Mineralogy of aeolian dust reaching the North Pacific Ocean 1. Sampling and analysis, J. Geophys. Res., 99, 21017–21023, doi:10.1029/94JD01735, 1994. 3500
Lieke, K., Kandler, K., Scheuvens, D., Emmel, C., Von Glahn, C., Petzold, A., Weinzierl, B., Veira, A., Ebert, M., Weinbruch, S., and Schütz, L: Particle chemical properties in the vertical column based on aircraft observations in the vicinity of Cape Verde Islands, Tellus B, 63, 497–511, doi:10.1111/j.1600-0889.2011.00553.x, 2011. 3496
Ma, Q., Liu, Y., Liua, C., and He, H.: Heterogeneous reaction of acetic acid on MgO, α-Al_2O_3, and $CaCO_3$ and the effect on the hygroscopic behaviour of these particles, Phys. Chem. Chem. Phys., 14, 8403–8409, doi:10.1039/C2CP40510E, 2012. 3495
Maher, B., Prospero, J., Mackie, D., Gaiero, D., Hesse, P., and Balkanski, Y.: Global connections between aeolian dust, climate and ocean biogeochemistry at the present day and at the

ACPD
15, 3493–3575, 2015

last glacial maximum, Earth-Sci. Rev., 99, 61–97, doi:10.1016/j.earscirev.2009.12.001, 2010. 3495
Marticorena, B.: Dust production mechanisms, in: Mineral Dust: A Key Player in the Earth System, edited by: Knippertz, P. and Stuut, J.-B., chap. 5, Springer Netherlands, Dordrecht, Heidelberg, New York, London, 93–120, doi:10.1007/978-94-017-8978-3_5, 2014. 3500, 3503
Marticorena, B., Bergametti, G., Gillette, D., and Belnap, J.: Factors controlling threshold friction velocity in semiarid and arid areas of the United States, J. Geophys. Res., 102, 23277–23287, doi:10.1029/97JD01303, 1997. 3499
Matsuki, A., Schwarzenboeck, A., Venzac, H., Laj, P., Crumeyrolle, S., and Gomes, L.: Cloud processing of mineral dust: direct comparison of cloud residual and clear sky particles during AMMA aircraft campaign in summer 2006, Atmos. Chem. Phys., 10, 1057–1069, doi:10.5194/acp-10-1057-2010, 2010. 3495
McFadden, L. D. and Hendricks, D. M.: Changes in the content and composition of pedogenic iron oxyhydroxides in a chronosequence of soils in southern California, Quaternary Res., 23, 189–204, doi:10.1016/0033-5894(85)90028-6, 1985. 3515
McTainsh, G. H., Lynch, A. W., and Hales, R.: Particle-size analysis of aeolian dusts, soils and sediments in very small quantities using a Coulter Multisizer, Earth Surf. Proc. Land., 22, 1207–1216, doi:10.1002/(SICI)1096-9837(199724)22:13<1207::AID-ESP820>3.0.CO;2-K, 1997. 3499
Mei, F., Zhang, X., Lu, H., Shen, Z., and Wang, Y.: Characterization of MASDs of surface soils in north China and its influence on estimating dust emission, Chin. Sci. Bull., 49, 2169–2176, doi:10.1007/BF03185784, 2004. 3499
Miller, R. L., Tegen, I., and Perlwitz, J.: Surface radiative forcing by soil dust aerosols and the hydrologic cycle, J. Geophys. Res., 109, D04203, doi:10.1029/2003JD004085, 2004. 3495
Miller, R. L., Cakmur, R. V., Perlwitz, J., Geogdzhayev, I. V., Ginoux, P., Koch, D., Kohfeld, K. E., Prigent, C., Ruedy, R., Schmidt, G. A., and Tegen, I.: Mineral dust aerosols in the NASA Goddard Institute for Space Sciences ModelE atmospheric general circulation model, J. Geophys. Res., 111, D06208, doi:10.1029/2005JD005796, 2006. 3497, 3505, 3517, 3519
Miller, R. L., Knippertz, P., García-Pando, C. P., Perlwitz, J. P., and Tegen, I.: Impact of dust radiative forcing upon climate, in: Mineral Dust – A Key Player in the Earth System, edited by: Knippertz, P. and Stuut, J.-B. W., Chap. 13, Springer Netherlands, Dordrecht, Heidelberg, New York, London, 327–357, doi:10.1007/978-94-017-8978-3_13, 2014 3495

ACPD
15, 3493–3575, 2015

Moosmüller, H., Engelbrecht, J. P., Skiba, M., Frey, G., Chakrabarty, R. K., and Arnott, W. P.: Single scattering albedo of fine mineral dust aerosols controlled by iron concentration, J. Geophys. Res., 117, D11210, doi:10.1029/2011JD016909, 2012. 3495, 3515

Murray, B. J., O'Sullivan, D., Atkinson, J. D., and Webb, M. E.: Ice nucleation by particles immersed in supercooled cloud droplets, Chem. Soc. Rev., 41, 6519–6554, doi:10.1039/C2CS35200A, 2012. 3495

Nickovic, S., Vukovic, A., Vujadinovic, M., Djurdjevic, V., and Pejanovic, G.: Technical Note: High-resolution mineralogical database of dust-productive soils for atmospheric dust modeling, Atmos. Chem. Phys., 12, 845–855, doi:10.5194/acp-12-845-2012, 2012. 3496, 3498, 3507, 3508, 3520, 3521, 3529, 3549, 3550

NRCS Soil Survey Staff: US General Soil Map (STATSGO), Natural Resources Conservation Service, United States Department of Agriculture, available online at http://sdmdataaccess.nrcs.usda.gov/, last access date: 11 April 2013, 2012. 3549

Pérez García-Pando, C., Stanton, M. C., Diggle, P. J., Trzaska, S., Miller, R. L., Perlwitz, J. P., Baldasano, J. M., Cuevas, E., Ceccato, P., Yaka, P., and Thomson, M. C.: Soil dust aerosols and wind as predictors of seasonal meningitis incidence in Niger, Environ. Health Perspect., 122, 679–686, doi:10.1289/ehp.1306640, 2014a. 3495

Pérez García-Pando, C., Thomson, M. C., Stanton, M. C., Diggle, P. J., Hopson, T., Pandya, R., Miller, R. L., and Hugonnet, S.: Meningitis and climate: from science to practice, Earth Persp., 1, 1–15, doi:10.1186/2194-6434-1-14, 2014b. 3495

Pérez García-Pando, C., Perlwitz, J. P., Miller, R. L., and Rodriguez, S.: Dust elemental composition at Izaña Observatory: modeling and observations, in preparation, 2015. 3497, 3503, 3533

Perlwitz, J. and Miller, R. L.: Cloud cover increase with increasing aerosol absorptivity: A counterexample to the conventional semidirect aerosol effect, J. Geophys. Res., 115, D08203, doi:10.1029/2009JD012637, 2010. 3495

Perlwitz, J. P., Pérez García-Pando, C., and Miller, R. L.: Predicting the mineral composition of dust aerosols – Part 2: Model evaluation and identification of key processes with observations, Atmos. Chem. Phys. Discuss., 15, 3577–3627, doi:10.5194/acpd-15-3577-2015, 2015. 3497, 3503, 3510, 3518, 3519, 3524, 3529, 3532, 3533

Prather, M. J.: Numerical advection by conservation of second-order moments, J. Geophys. Res., 91, 6671–6681, doi:10.1029/JD091iD06p06671, 1986. 3518

ACPD
15, 3493–3575, 2015

Prigent, C., Tegen, I., Aires, F., Marticorena, B., and Zribi, M.: Estimation of the aerodynamic roughness length in arid and semi-arid regions over the globe with the ERS scatterometer, J. Geophys. Res., 110, D09205, doi:10.1029/2004JD005370, 2005. 3518

Rayner, N. A., Parker, D. E., Horton, E. B., Folland, C. K., Alexander, L. V., Rowell, D. P., Kent, E. C., and Kaplan, A.: Global analyses of sea surface temperature, sea ice, and night marine air temperature since the late nineteenth century, J. Geophys. Res., 108, 4407, doi:10.1029/2002JD002670, 2003. 3519

Redmond, H. E., Dial, K. D., and Thompson, J. E.: Light scattering and absorption by wind blown dust: Theory, measurement, and recent data, Aeolian Res., 2, 5–26, doi:10.1016/j.aeolia.2009.09.002, 2010. 3495

Reid, E. A., Reid, J. S., Meier, M. M., Dunlap, M. R., Cliff, S. S., Broumas, A., Perry, K., and Maring, H.: Characterization of African dust transported to Puerto Rico by individual particle and size segregated bulk analysis, J. Geophys. Res., 108, 22 pp., doi:10.1029/2002JD002935, 2003. 3496, 3500, 3516

Reynolds, C. A., Jackson, T. J., and Rawls, W. J.: Estimating soil water-holding capacities by linking the Food and Agriculture Organization Soil map of the world with global pedon databases and continuous pedotransfer functions, Water Resour. Res., 36, 3653–3662, doi:10.1029/2000WR900130, 2000. 3498

Rodríguez, S., Alastuey, A., Alonso-Pérez, S., Querol, X., Cuevas, E., Abreu-Afonso, J., Viana, M., Pérez, N., Pandolfi, M., and de la Rosa, J.: Transport of desert dust mixed with North African industrial pollutants in the subtropical Saharan Air Layer, Atmos. Chem. Phys., 11, 6663–6685, doi:10.5194/acp-11-6663-2011, 2011. 3519

Rubasinghege, G., Ogden, S., Baltrusaitis, J., and Grassian, V. H.: Heterogeneous uptake and adsorption of gas-phase formic acid on oxide and clay particle surfaces: the roles of surface hydroxyl groups and adsorbed water in formic acid adsorption and the impact of formic acid adsorption on water uptake, J. Phys. Chem. A, 117, 11316–11327, doi:10.1021/jp408169w, 2013. 3495

Russell, L. M., Maria, S. F., and Myneni, S. C. B.: Mapping organic coatings on atmospheric particles, Geophys. Res. Lett., 29, 1779, doi:10.1029/2002GL014874, 2002. 3495

Sassen, K.: Indirect climate forcing over the western US from Asian dust storms, Geophys. Res. Lett., 29, 1465, doi:10.1029/2001GL014051, 2002. 3495

Scanza, R. A., Mahowald, N., Ghan, S., Zender, C. S., Kok, J. F., Liu, X., Zhang, Y., and Albani, S.: Modeling dust as component minerals in the Community Atmosphere Model: de-

ACPD
15, 3493–3575, 2015

velopment of framework and impact on radiative forcing, Atmos. Chem. Phys., 15, 537–561, doi:10.5194/acp-15-537-2015, 2015. 3496, 3497, 3502, 3505, 3512, 3513, 3534

Scheuvens, D. and Kandler, K.: On composition, morphology, and size distribution of airborne mineral dust, in: Mineral Dust: A Key Player in the Earth System, edited by: Knippertz, P., and Stuut, J.-B., chap. 2, Springer Netherlands, Dordrecht, Heidelberg, New York, London, 15–49, doi:10.1007/978-94-017-8978-3_2, 2014. 3496, 3499, 3501, 3517

Scheuvens, D., Kandler, K., Küpper, M., Lieke, K., Zorn, S., Ebert, M., Schütz, L., and Weinbruch, S.: Individual-particle analysis of airborne dust samples collected over Morocco in 2006 during SAMUM 1, Tellus B, 63, 512–530, doi:10.1111/j.1600-0889.2011.00554.x, 2011. 3496, 3502

Schmidt, G. A., Kelley, M., Nazarenko, L., Ruedy, R., Russell, G. L., Aleinov, I., Bauer, M., Bauer, S. E., Bhat, M. K., Bleck, R., Canuto, C., Chen, Y.-H., Cheng, Y., Clune, T. L., Del Genio, A., de Fainchtein, R., Faluvegi, G., Hansen, J. E., Healy, R. J., Kiang, N. Y., Koch, D., Lacis, A. A., LeGrande, A. N., Lerner, J., Lo, K. K., Matthews, E. E., Menon, S., Miller, R. L., Oinas, V., Oloso, A. O., Perlwitz, J. P., Puma, M. J., Putman. W. P., Rind, D., Romanou, A., Sato, M., Shindell, D. T., Sun, S., Syed, R. A., Tausnev, N., Tsigaridis, K., Unger, N., Voulgarakis, A., Yao, M.-S., and Zhang, J.: Configuration and assessment of the GISS ModelE2 contributions to the CMIP5 archive, J. Adv. Model. Earth Syst., 6, 141–184, doi:10.1002/2013MS000265, 2014. 3517

Schulz, M., Prospero, J. M., Baker, A. R., Dentener, F., Ickes, L., Liss, P. S., Mahowald, N. M., Nickovic, S., Pérez García-Pando, C., Rodríguez, S., Sarin, M., Tegen, I., and Duce, R. A.: Atmospheric transport and deposition of mineral dust to the ocean: implications for research needs, Environ. Sci. Technol., 46, 10390–10404, doi:10.1021/es300073u, 2012. 3495

Seifert, P., Ansmann, A., Mattis, I., Wandinger, U., Tesche, M., Engelmann, R., Müller, D., Pérez, C., and Haustein, K.: Saharan dust and heterogeneous ice formation: eleven years of cloud observations at a central European EARLINET site, J. Geophys. Res.-Atmos., 115, D20201, doi:10.1029/2009JD013222, 2010. 3495

Shangguan, W., Dai, Y., Duan, Q., Liu, B., and Yuan, H.: A global soil data set for earth system modeling, J. Adv. Model. Earth Syst., 6, 249–263, doi:10.1002/2013MS000293, 2014. 3498, 3499

Shao, Y.: A model for mineral dust emission, J. Geophys. Res., 106, 20239–20254, doi:10.1029/2001JD900171, 2001. 3496, 3498, 3503, 3504

ACPD
15, 3493–3575, 2015

Shao, Y., Raupach, M. R., and Findlater, P. A.: Effect of saltation bombardment on the entrainment of dust by wind, J. Geophys. Res., 98, 12,719–12,726, doi:10.1029/93JD00396, 1993. 3500

Shao, Y., Raupach, M. R., and Leys, J. F.: A model for predicting aeolian sand drift and dust entrainment on scales from paddock to region, Aust. J. Soil Res., 34, 309–342, doi:10.1071/SR9960309, 1996. 3518

Shi, Z., Krom, M. D., Jickells, T. D., Bonneville, S., Carslaw, K. S., Mihalopoulos, N., Baker, A. R., and Benning, L. G.: Impacts on iron solubility in the mineral dust by processes in the source region and the atmosphere: a review, Aeolian Res., 5, 21–42, doi:10.1016/j.aeolia.2012.03.001, 2012. 3495, 3507, 3515, 3516

Shi, Z. B., Woodhouse, M. T., Carslaw, K. S., Krom, M. D., Mann, G. W., Baker, A. R., Savov, I., Fones, G. R., Brooks, B., Drake, N., Jickells, T. D., and Benning, L. G.: Minor effect of physical size sorting on iron solubility of transported mineral dust, Atmos. Chem. Phys., 11, 8459–8469, doi:10.5194/acp-11-8459-2011, 2011. 3495

Sokolik, I. N. and Toon, O. B.: Direct radiative forcing by anthropogenic airborne mineral aerosols, Nature, 381, 681–683, doi:10.1038/381681a0, 1996. 3495

Sokolik, I. N. and Toon, O. B.: Incorporation of mineralogical composition into models of the radiative properties of mineral aerosol from UV to IR wavelengths, J. Geophys. Res., 104, 9423–9444, doi:10.1029/1998JD200048, 1999. 3495, 3515, 3528

Sow, M., Alfaro, S. C., Rajot, J. L., and Marticorena, B.: Size resolved dust emission fluxes measured in Niger during 3 dust storms of the AMMA experiment, Atmos. Chem. Phys., 9, 3881–3891, doi:10.5194/acp-9-3881-2009, 2009. 3496, 3503, 3504

Sullivan, R. C., Guazzotti, S. A., Sodeman, D. A., Tang, Y., Carmichael, G. R., and Prather, K. A.: Mineral dust is a sink for chlorine in the marine boundary layer, Atmos. Environ., 41, 7166–7179, doi:10.1016/j.atmosenv.2007.05.047, 2007. 3495

Takahashi, Y., Higashi, M., Furukawa, T., and Mitsunobu, S.: Change of iron species and iron solubility in Asian dust during the long-range transport from western China to Japan, Atmos. Chem. Phys., 11, 11237–11252, doi:10.5194/acp-11-11237-2011, 2011. 3495

Tegen, I. and Fung, I.: Modeling of mineral dust in the atmosphere: Sources, transport, and optical thickness, J. Geophys. Res., 99, 22897–22914, doi:10.1029/94JD01928, 1994. 3519

Tegen, I., Hollrig, P., Chin, M., Fung, I., Jacob, D., and Penner, J.: Contribution of different aerosol species to the global aerosol extinction optical thickness: estimates from model results, J. Geophys. Res., 102, 23895–23915, doi:10.1029/97JD01864, 1997. 3495

ACPD
15, 3493–3575, 2015

Turner, D. D.: Ground-based infrared retrievals of optical depth, effective radius, and composition of airborne mineral dust above the Sahel, J. Geophys. Res., 113, D00E03, doi:10.1029/2008JD010054, 2008. 3495

Twohy, C. H., Kreidenweis, S. M., Eidhammer, T., Browell, E. V., Heymsfield, A. J., Bansemer, A. R., Anderson, B. E., Chen, G., Ismail, S., DeMott, P. J., and Heever, S. C. V. D.: Saharan dust particles nucleate droplets in eastern Atlantic clouds, Geophys. Res. Lett., 36, L01807, doi:10.1029/2008GL035846, 2009. 3495

Usher, C. R., Michel, A. E., Stec, D., and Grassian, V. H.: Laboratory studies of ozone uptake on processed mineral dust, Atmos. Environ., 37, 5337–5347, doi:10.1016/j.atmosenv.2003.09.014, 2003. 3495

Wagner, R., Ajtai, T., Kandler, K., Lieke, K., Linke, C., Müller, T., Schnaiter, M., and Vragel, M.: Complex refractive indices of Saharan dust samples at visible and near UV wavelengths: a laboratory study, Atmos. Chem. Phys., 12, 2491–2512, doi:10.5194/acp-12-2491-2012, 2012. 3495, 3515

Washington, R., Bouet, C., Cautenet, G., Mackenzie, E., Ashpole, I., Engelstaedter, S., Lizcano, G., Henderson, G. M., Schepanski, K., and Tegen, I.: Dust as a tipping element: the Bodélé Depression, Chad, P. Natl. Acad. Sci. USA, 106, 20564–20571, doi:10.1073/pnas.0711850106, 2009. 3534

Webb, R. S., Rosenzweig, C. E., and Levine, E. R.: Specifying land surface characteristics in general circulation models: Soil profile data set and derived water-holding capacities, Global Biogeochem. Cy., 7, 97–108, doi:10.1029/92GB01822, 1993. 3498

Wesely, M. L. and Hicks, B. B.: Some factors that affect the deposition rates of sulfur dioxide and similar gases on vegetation, J. Air Pollut. Control Assoc., 27, 1110–1116, doi:10.1080/00022470.1977.10470534, 1977. 3519

Yakobi-Hancock, J. D., Ladino, L. A., and Abbatt, J. P. D.: Feldspar minerals as efficient deposition ice nuclei, Atmos. Chem. Phys., 13, 11175–11185, doi:10.5194/acp-13-11175-2013, 2013. 3495

Zimmermann, F., Weinbruch, S., Schütz, L., Hofmann, H., Ebert, M., Kandler, K., and Worringen, A.: Ice nucleation properties of the most abundant mineral dust phases, J. Geophys. Res., 113, D23204, doi:10.1029/2008JD010655, 2008. 3495

ACPD
15, 3493–3575, 2015

Table 1. Datasets used in this study.

Name and Reference	Description
Mean Mineralogical Table (MMT) (Claquin et al., 1999)	Mineral fractions of clay and silt soil particles for 25 FAO arid soil types. The MMT was expanded with 3 additional soil types (Yermosols, Haplic Yermosols and Xerosols) whose mineral fractions were extrapolated by Nickovic et al. (2012) from similar types.
Digital Soil Map of the World (DMSW) (FAO, 2007; FAO/IIASA/ISRIC/ISSCAS/JRC, 2012) www.fao.org/geonetwork/srv/en/metadata.show?id=14116	Geographical distribution of 137 soil types with a resolution of $5' \times 5'$ latitude by longitude. The MMT uses 28 arid soil types to assign mineral fractions to the clay and silt-sized fractions of the soil.
Hybrid STATSGO/FAO (FAO/IIASA/ISRIC/ISSCAS/JRC, 2012; NRCS Soil Survey Staff, 2012) www.ral.ucar.edu/research/land/technology/lsm.php	Geographical distribution of soil texture classes (see Table 3). The FAO global soil texture maps at $5' \times 5'$ latitude by longitude are remapped onto a global $30'' \times 30''$ latitude by longitude grid. Within Contiguous United States (CONUS), the soil texture is replaced by the $30'' \times 30''$ STATSGO data.
Dust and mineral measurements at Tinfou, Morocco (Kandler et al., 2009)	Measurements of dust number and mineral volume for 10 size bins extending to 250 µm at Tinfou, Morocco during the SAMUM campaign in 2006.

ACPD
15, 3493–3575, 2015

Table 2. Minerals represented in ModelE. Closed circles (•) denote minerals identified in wet-sieved soils by Claquin et al. (1999). Stars (⋆) denote iron oxide extrapolated to clay sizes by Nickovic et al. (2012). Open circles (∘) denote minerals restored to silt sizes that were disaggregrated by wet sieving. Triangles (▷) denote minerals introduced at clay sizes as suggested by measurements at Tinfou, Morocco during SAMUM (Kandler et al., 2009).

Mineral	Disturbed soil		Undisturbed soil &dust	
	Clay	Silt	Clay	Silt
Illite	•		•	∘
Kaolinite	•		•	∘
Smectite	•		•	∘
Quartz	•	•	•	•
Carbonates	•	•	•	•
Gypsum		•	▷	•
Feldspar		•	▷	•
Iron Oxides	⋆	•	⋆	•

ACPD
15, 3493–3575, 2015

Table 3. Soil texture classes with sand, silt, and clay percentages, and clay (s^c) and silt (s^s) mass fractions (relative to clay plus silt) in the Hybrid STATSGO/FAO soil texture data base that are used for the derivation of the mineral fractions.

Class	Texture	Sand (%)	Silt (%)	Clay (%)	s^c	s^s
1	Sand	92	5	3	0.38	0.62
2	Loamy Sand	82	12	6	0.33	0.67
3	Sandy Loam	58	32	10	0.24	0.76
4	Silt Loam	17	70	13	0.16	0.84
5	Silt	10	85	5	0.06	0.94
6	Loam	43	39	18	0.32	0.68
7	Sandy Clay Loam	58	15	27	0.64	0.36
8	Silty Clay Loam	10	56	34	0.38	0.62
9	Clay Loam	32	34	34	0.5	0.5
10	Sandy Clay	52	6	42	0.88	0.12
11	Silty Clay	6	47	47	0.5	0.5
12	Clay	22	20	58	0.74	0.26

ACPD
15, 3493–3575, 2015

Table 4. Size categories for dust transported in ModelE. *k*-index is subscript denoting the particle size of the soil and emitted mass fractions. Note that the sixth size category (comprised of the largest particles) is not transported, and exists solely to match the diameter range corresponding to the MMT.

Diameter (μm)	*k*-index
Clay	
0.1–2	1
Silt	
2–4	2
4–8	3
8–16	4
16–32	5
32–50	6

ACPD
15, 3493–3575, 2015

Table 5. List of symbols used to represent mass fractions of soil and emitted minerals (Sect. 2.2.1).

a	soil type
b	soil texture
s^{c}	mass fraction of clay-sized soil particles relative to total clay and silt (Table 3)
s^{s}	mass fraction of silt-sized soil particles relative to total clay and silt (Table 3)
f_n^{c}	mass fraction of soil mineral n (relative to clay-sized minerals)
f_n^{n}	mass fraction of soil mineral n (relative to silt-sized minerals)
s_n^{c}	mass fraction of soil mineral n at clay sizes
s_n^{s}	mass fraction of soil mineral n at silt sizes
d^{c}	mass fraction of emitted clay-sized dust
d^{s}	mass fraction of emitted silt-sized dust
d_n^{c}	mass fraction of emitted mineral n at clay sizes
d_n^{s}	mass fraction of emitted mineral n at silt sizes
γ	parameter controlling reaggregation of emitted silt particles from wet-sieved clay particles
η	parameter related to reaggregation
$m_{n,k}$	mass fraction of mineral n within size category k (normalized using only silt sizes)

ACPD
15, 3493–3575, 2015

Table 6. List of symbols used to represent mixtures of iron oxide and other minerals (Sect. 2.2.2).

$d_{n,k}$	mass fraction of mineral n in size class k
$d_{n,k}^{\text{pure}}$	mass fraction of uncombined mineral n in size class k (excluding iron oxide)
$d_{n,k}^{\text{mix}}$	mass fraction of mineral n with mixed with iron oxide
$d_{\text{Fe},k}$	mass fraction of iron oxide in size class k
$d_{\text{Fe},k}^{\text{pure}}$	mass fraction of pure crystalline iron oxide k
$d_{\text{Fe},k}^{\text{mix}}$	mass fraction of iron oxide mixed with other minerals
$d_{\text{Fe}\|n,k}^{\text{mix}}$	mass fraction of iron oxide mixed with mineral n
ϵ	fraction of iron oxide not available for mixing
ϵ_0	Coefficient of proportionality between $d_{\text{Fe},k}$ and ϵ
R	fraction of mixed particle mass contributed by iron oxide
$\overline{d}_k$	mass fraction of all non-iron oxide minerals in size class k

ACPD
15, 3493–3575, 2015

Table 7. Globally averaged dust emission, load and lifetime. The number in parentheses is one SD of interannual variability

	SMF		AMF	
Emission [Tg a^{-1}]				
Clay (0–2 µm)	920		44	
Silt (2–16 µm)	657		1049	
Total (< 16 µm)	1577	(±70)	1094	(±49)
Silt (16–32 µm)	647		1131	
Total (< 32 µm)	2224	(±100)	2224	(±100)
Load [Tg]				
Clay (0–2 µm)	14.60		0.71	
Silt (2–16 µm)	4.66		7.31	
Total (< 16 µm)	19.26	(±0.73)	8.02	(±0.29)
Silt (16–32 µm)	0.46		0.81	
Total (< 32 µm)	19.72	(±0.74)	8.83	(±0.31)
Lifetime (< 16 µm) [d]				
Emission	4.45		2.68	
Wet Deposition	8.35		8.87	
Gravitational Settling	19.05		5.07	
Turbubulent Deposition	20.44		16.35	
Lifetime (< 32 µm) [d]				
Emission	3.24		1.45	
Wet Deposition	8.41		9.08	
Gravitational Settling	7.40		1.98	
Turbubulent Deposition	19.23		14.01	

ACPD
15, 3493–3575, 2015

Table 8. Mineral densities in $10^3\,kg\,m^{-3}$. The densities of illite and smectite are an average of their individual values, since they are often found interleaved. Feldspar density is taken from plagioclase. The iron oxide density is an average of hematite and goethite. The densities were taken from http://www.mindat.org and http://www.webmineral.com.

Mineral	Density
Illite	2.57
Kaolinite	2.63
Smectite	2.57
Calcite	2.71
Quartz	2.67
Feldspar	2.68
Iron oxides	4.77

ACPD
15, 3493–3575, 2015

Table 9. List of experiments. (SD = size distribution)

Experiment Name	Comment
SMF	Control (no reaggregation; emitted SD from local soil texture)
AMF	Default reaggregation parameter (γ = 2); emitted SD from measurements
AMF (γ = 0)	No reaggregation
AMF (γ = 3.5)	Increased reaggregation
AMF-NoFeAcc	No internal mixtures of iron oxide with other minerals (γ = 2)
SMF-NoClayFe	No clay-sized iron oxide

ACPD
15, 3493–3575, 2015

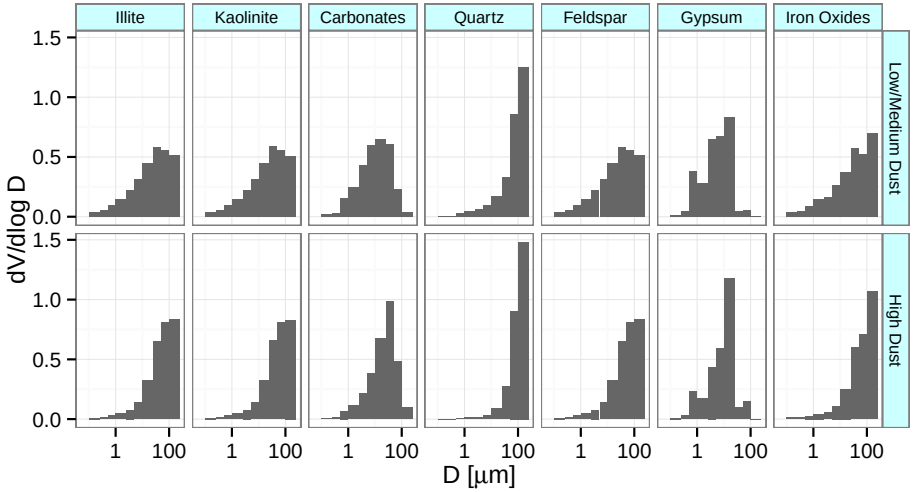

Figure 1. Volume distribution of minerals with respect to particle diameter, calculated from size-resolved measurements of dust number and volume fraction by Kandler et al. (2009). (Phyllosilicates and feldspar are assumed by that study to have identical volume fractions due to the similar measurement properties of these minerals.) The size bins correspond to the following range of particle diameter (µm): 0.1–0.25; 0.25–0.5; 0.5–1.0; 1.0–2.5; 2.5–5.0; 5.0–10.0; 10.0–25.0; 25.0–50.0; 50.0–100.0.; 100.0–250.0. Upper panel: low/medium dust concentration; lower panel: high dust concentration. The size distribution is normalized so that the total volume is unity for each mineral.

ACPD
15, 3493–3575, 2015

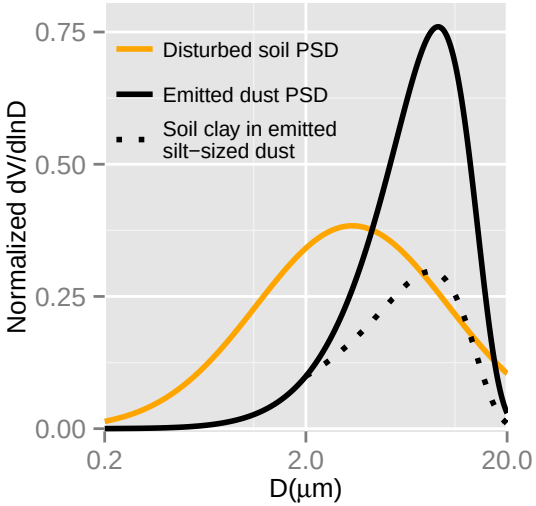

Figure 2. Size distribution of emitted dust (black line) derived from Eq. (1) with λ = 12 µm (Kok, 2011). The orange curve describes the arid dispersed soil used in the calculation of $U(D)$ in Eq. (1), and is represented by a monomodal log-normal distribution with a volume median diameter of 3.4 µm and geometric SD of 3.0. Both curves are and normalized over the range 0–20 µm. The dotted line represents the contribution of dispersed soil clay particles to silt-sized dust aggregates calculated with Eq. (1) and in this example contributes 45 % of the emitted silt.

ACPD
15, 3493–3575, 2015

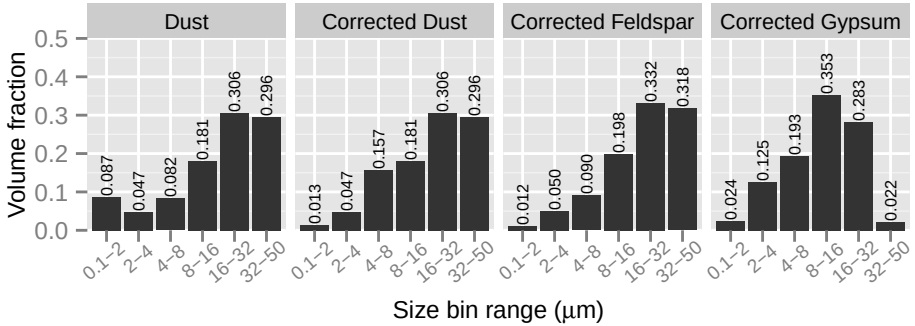

Figure 3. (From left to right) Distribution of dust volume calculated from measurements by Kandler et al. (2009); same but with corrected ratio of clay to silt (up to 20 μm) using Eq. (1) (cf. Kok, 2011); distribution of feldspar volume calculated from measurements by Kandler et al. (2009) but with same correction based on Kok (2011); same for gypsum. Each distribution is projected onto the ModelE transport bins (Table 4). A fifth "virtual" transport bin for diameters between 32 and 50 μm is added so that the total diameter range corresponds to that of the MMT. Each distribution is normalized over the entire diameter range.

ACPD
15, 3493–3575, 2015

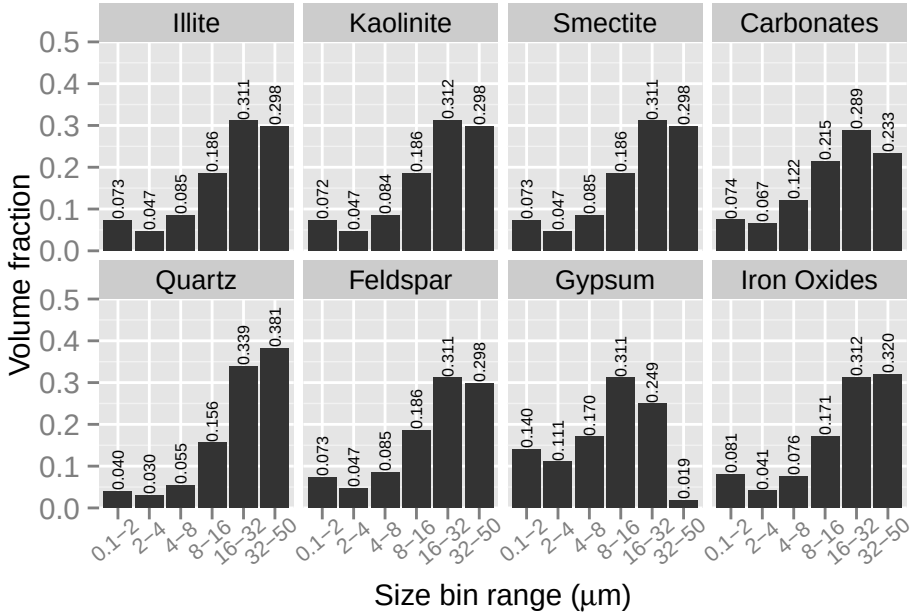

Figure 4. Fractional distribution of volume within the ModelE size bins for the minerals in Table 2, calculated from measurements by Kandler et al. (2009). A fifth "virtual" transport bin for diameters between 32 and 50 µm is added so that the total diameter range corresponds to that of the MMT. The distribution of each mineral is normalized separately over the entire diameter range.

ACPD
15, 3493–3575, 2015

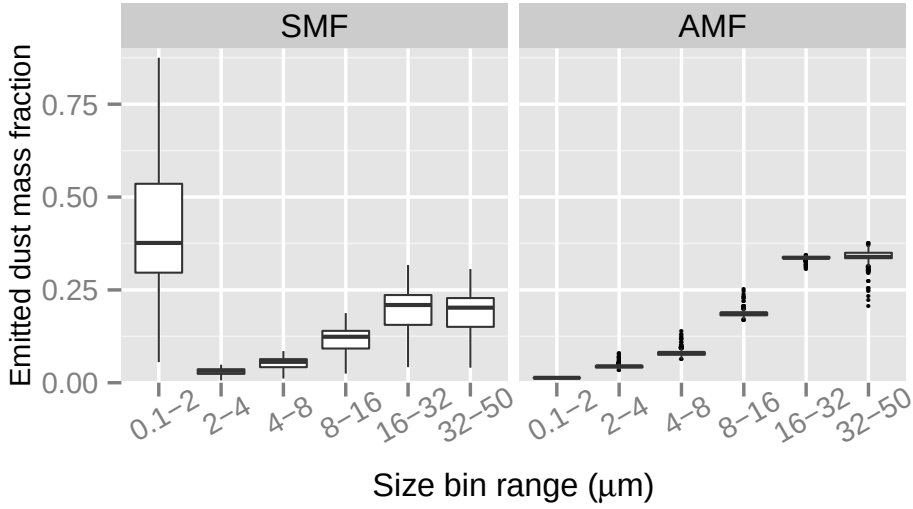

Figure 5. The distribution of the dust volume fraction over the ModelE size bins for the soil mineral fraction (SMF) method (left) and the aerosol mineral fraction (AMF) method (right). Within each size bin, the box plots depict variations related to combinations of soil texture and the 28 arid soil types included in the MMT. For each combination, the sum over all sizes is one. At each bin, each combination within the distribution is weighted by the total emission (at all sizes) to emphasize prolific sources. Each box shows the range in which the central 50 % of the data fall. The box borders show the first and third quartiles and the crossbar shows the median. Outliers exceeding the quartile values by more than a factor of 1.5, the interquartile distance, are marked as points.

ACPD
15, 3493–3575, 2015

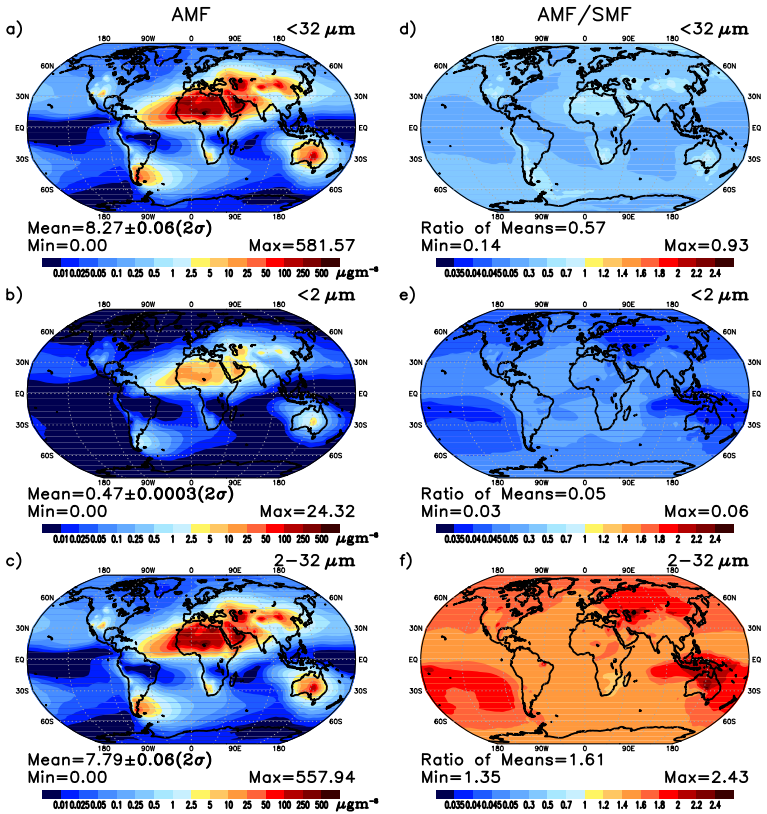

Figure 6. (Left panels) Annual-average surface concentration (summed over all minerals) for the AMF method and (right panels) the ratio of the AMF and SMF concentrations for: **(a, d)** total dust; **(b, e)** clay-sized dust; and **(c, f)** silt-sized dust.

ACPD
15, 3493–3575, 2015

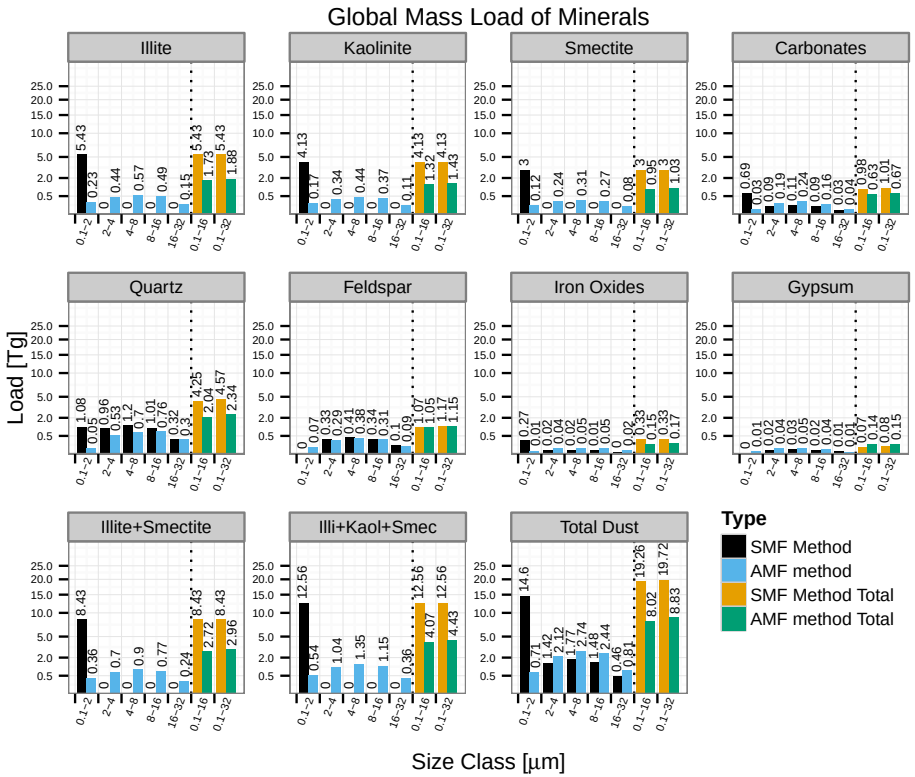

Figure 7. Global annual load (Tg) for the AMF and SMF experiments.

ACPD
15, 3493–3575, 2015

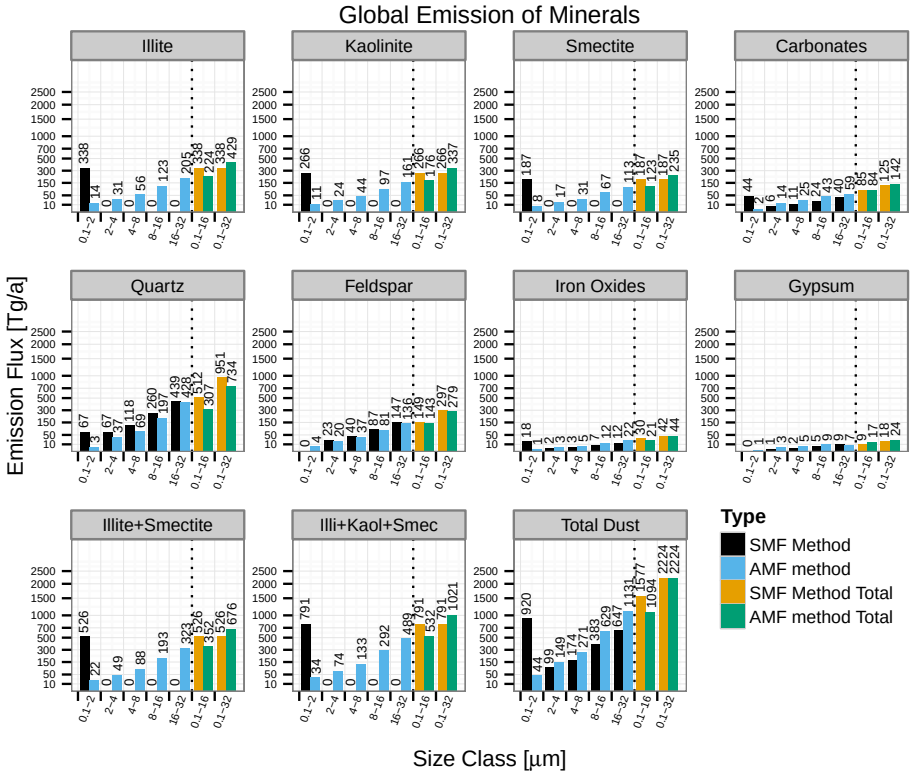

Figure 8. Global annual emission (Tg) for the AMF and SMF experiments.

ACPD
15, 3493–3575, 2015

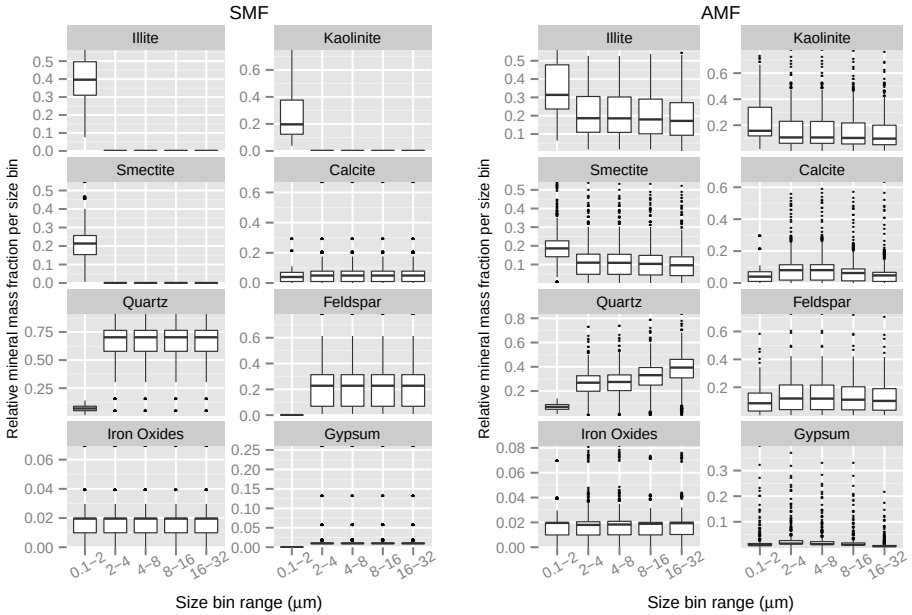

Figure 9. Relative mass fraction of each mineral in each size bin for the soil mineral fraction (SMF) method (left panels) and the aerosol mineral fraction (AMF) method. The box plots are constructed as in Fig. 5.

ACPD
15, 3493–3575, 2015

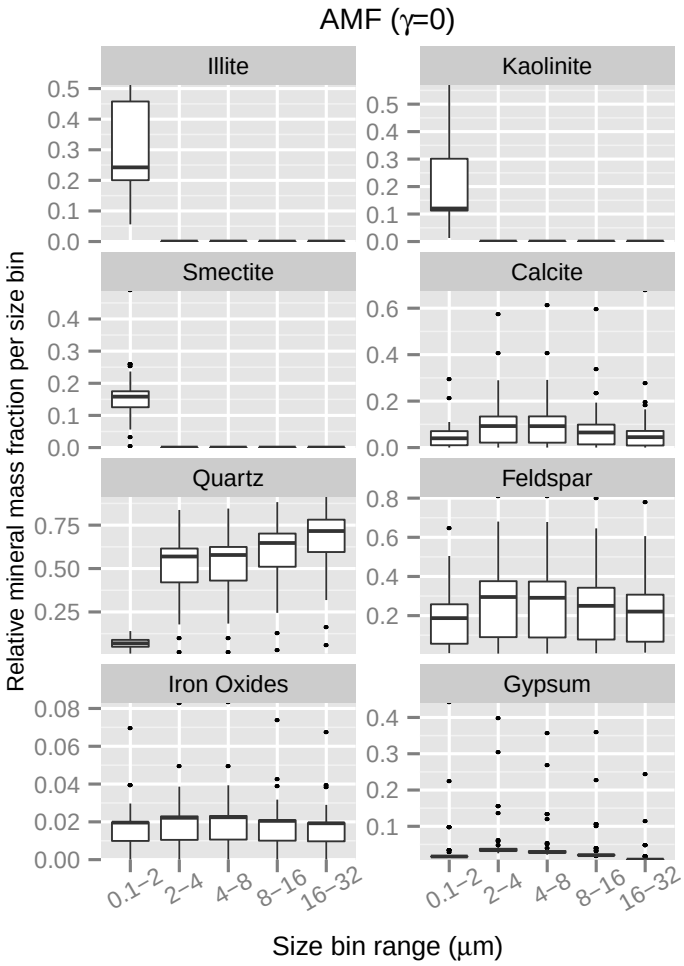

Figure 10. Same as Fig. 9 but for the aerosol mineral fraction (AMF) method with $\gamma = 0$.

ACPD
15, 3493–3575, 2015

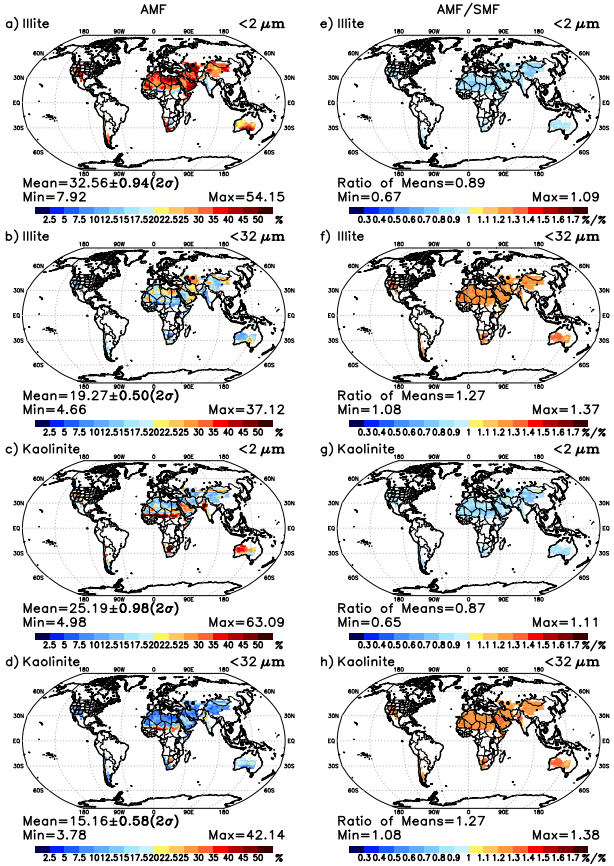

Figure 11. Annual-average fraction of emission of **(a, b)** illite and **(c, d)** kaolinite at clay and all sizes for the aerosol mineral fraction (AMF) method. The right column shows the ratio of fractional emission for the AMF and soil mineral fraction (SMF) methods for **(e, f)** illite and **(g, h)** kaolinite.

ACPD
15, 3493–3575, 2015

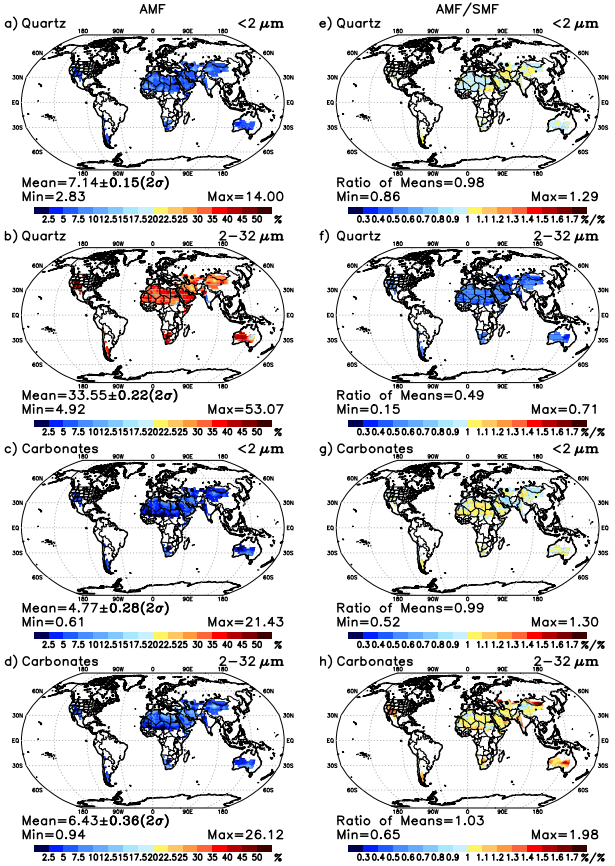

Figure 12. Fractional emission as in Fig. 11 but for clay and silt-sized quartz and carbonates.

ACPD
15, 3493–3575, 2015

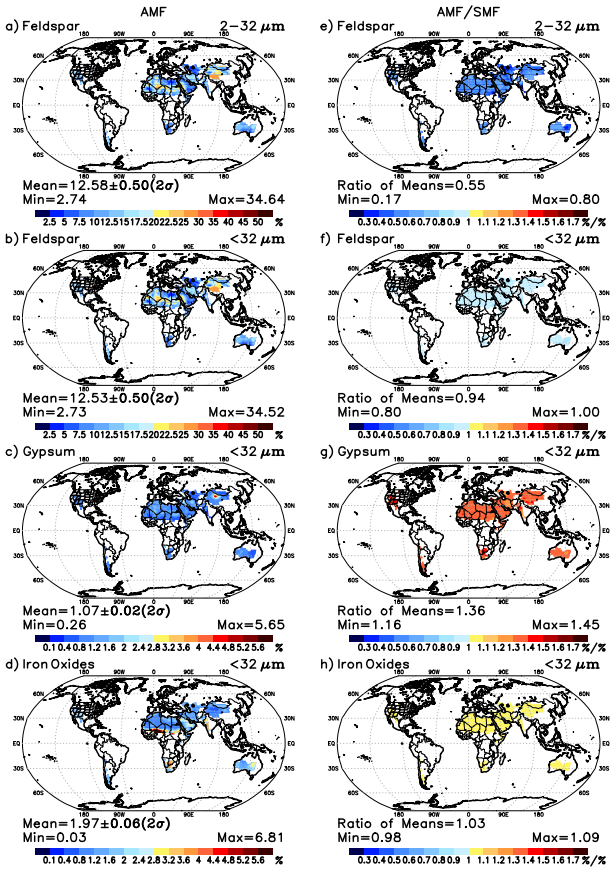

Figure 13. Fractional emission as in Fig. 11 but for feldspar (silt-sized and total), gypsum and iron oxides.

ACPD
15, 3493–3575, 2015

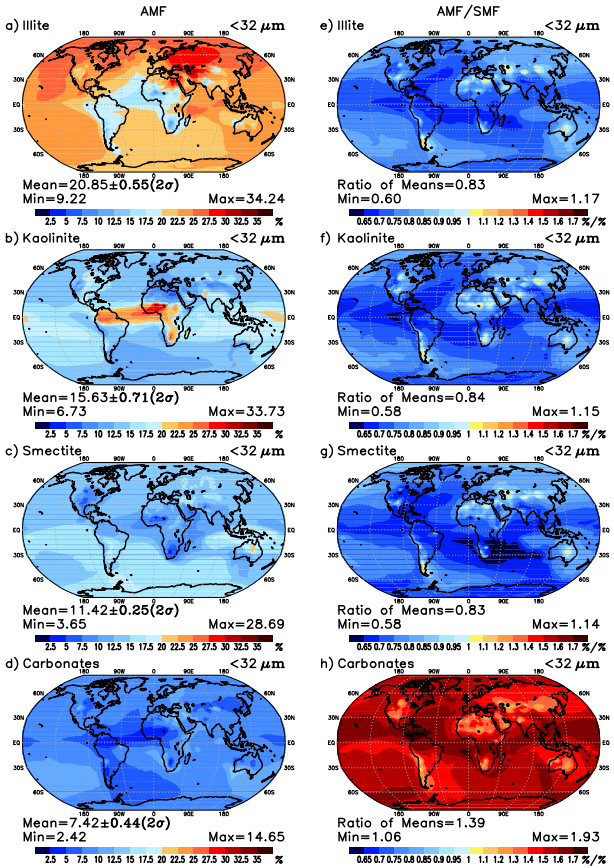

Figure 14. Annual-average fraction of surface concentration for **(a)** illite, **(b)** kaolinite, **(c)** smectite, and **(d)** carbonates for the AMF method. The right column shows the ratio between the AMF and the SMF fractions for **(e)** illite, **(f)** kaolinite, **(g)** smectite, and **(h)** carbonates.

ACPD
15, 3493–3575, 2015

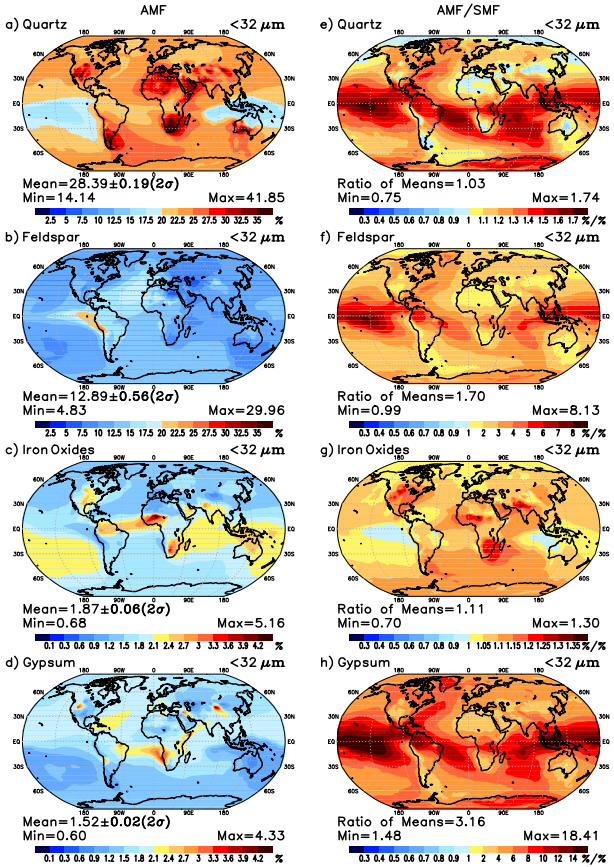

Figure 15. Fractional surface concentration as in Fig. 14 but for **(a, e)** quartz, **(b, f)** feldspar, **(c, g)** iron oxides, and **(d, h)** gypsum.

ACPD
15, 3493–3575, 2015

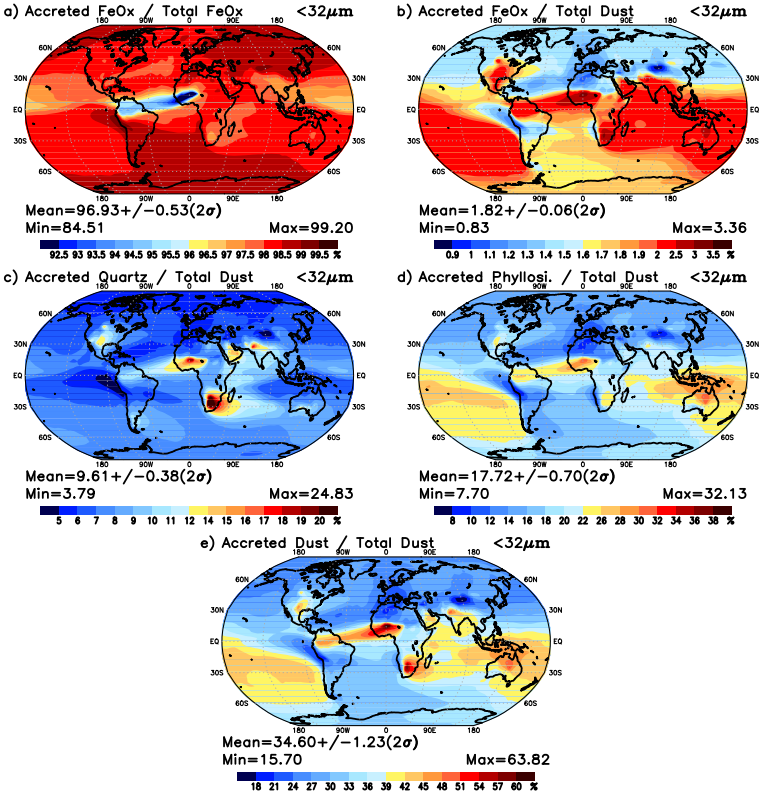

Figure 16. Annual-average column mass fraction of **(a)** accreted iron oxide relative to total iron oxide, and (relative to total dust) accreted **(b)** iron oxide, **(c)** quartz, **(d)** phyllosilicate (illite + kaolinite + smectite) and **(e)** dust.

ACPD
15, 3493–3575, 2015

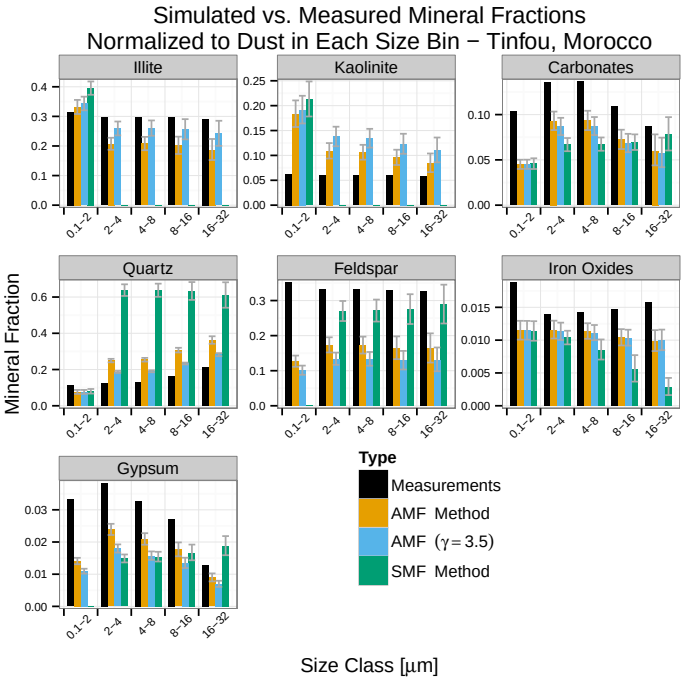

Figure 17. Mineral fractions of surface concentration relative to total dust concentration at Tinfou, Morocco. Measured values are calculated from volume fractions of minerals and number of total dust particles provided by Kandler et al. (2009) along with mineral densities from Table 8. Model values are from the SMF, AMF and AMF ($\gamma = 3.5$) experiments. The sum of mineral fractions within each size bin equals 1. Smectite is not included as it is not distinguished by the measurements. The uncertainty bars correspond to two standard errors.

ACPD
15, 3493–3575, 2015

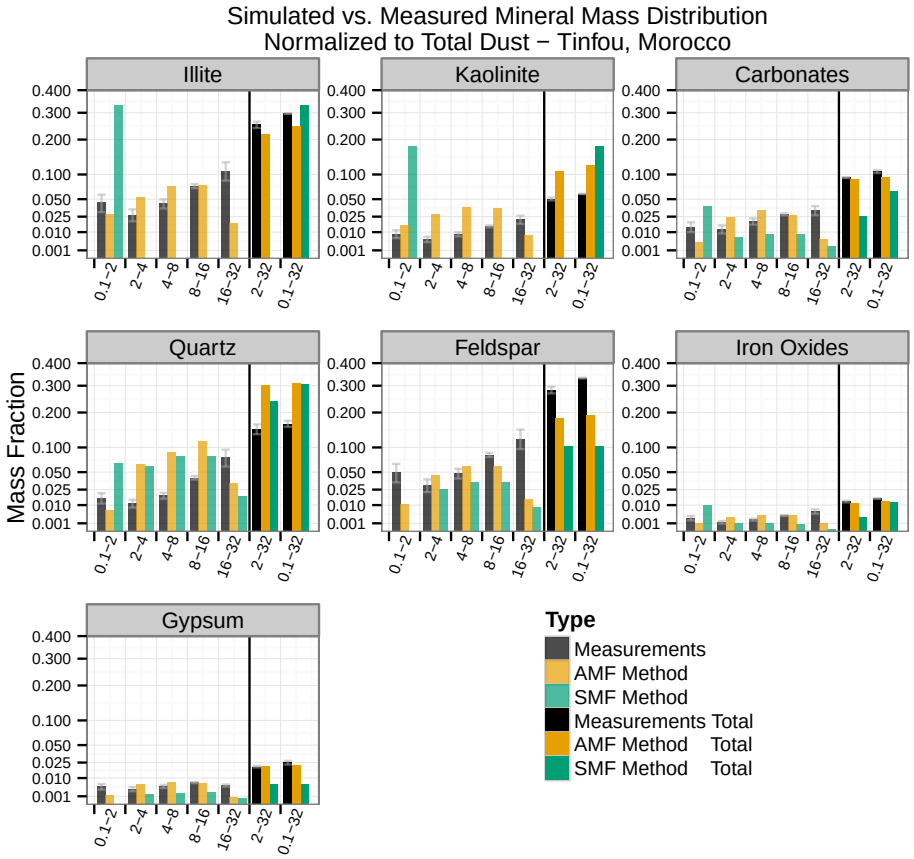

Figure 18. Same as Fig. 17 but the mineral fractions are relative to the total dust concentration, so that the sum over all mineral fractions and all size bins equals 1.

ACPD
15, 3493–3575, 2015